Roma Tre University

Mathematics and Physics Department

XXIX Doctorate School in Physics

Measurement of the rare decay $K_{\mathrm{S}} \to \pi^+\pi^0\pi^-$ with the KLOE detector

Candidate:
Alessandro Di Cicco

Supervisor:
Prof. Filippo Ceradini

Contents

Introduction **i**

1 Neutral kaon decays and $\mathcal{CP}$-symmetry violation **1**

1.1 Neutral kaon mass eigenstates and $\mathcal{CP}$ symmetry 3

1.2 $\mathcal{CP}$ violation in $K \to \pi\pi$ decays 4

1.3 $\mathcal{CP}$ violation in $K \to \pi\pi\pi$ decays 7

1.4 Dalitz plot analysis and current measurements of $\mathscr{B}^{cons}(K_S \to \pi^+\pi^0\pi^-)$ 9

1.5 Motivations for the measurement of the rare decay $K_S \to \pi^+\pi^0\pi^-$ . . 12

2 The KLOE experiment at DAΦNE **15**

2.1 The DAΦNE collider 15

2.2 The KLOE detector 17

2.2.1 The Drift Chamber 17

2.2.2 The Electromagnetic Calorimeter 20

2.2.3 The trigger system 23

2.2.4 Data acquisition 24

2.3 Data reconstruction 25

2.3.1 Cluster reconstruction 25

2.3.2 Track reconstruction 26

2.3.3 Track-to-cluster association 27

2.3.4 Event classification 28

2.4 Beam parameters and luminosity measurements 28

3 Event selection **31**

3.1 Simulations of signal and background 31

3.2 The K_S tag at KLOE 32

3.2.1 Identification of K_{L}-meson interactions in the calorimeter . . . 33
3.2.2 K_{L} and K_{S} momentum estimate 37
3.3 Considerations on background 37
3.4 Signal selection 39

4 Data analysis **41**
4.1 Background rejection 41
4.1.1 $\pi^0 \to \gamma\gamma$ reconstruction 42
4.1.2 β^* acceptance window 44
4.1.3 The three-pion invariant mass 46
4.2 Signal and control regions 48

5 Determination of the branching ratio **55**
5.1 Data analysis summary 55
5.2 Estimate of signal yield in the signal region 56
5.3 Background-hypothesis fit in the signal region 60
5.4 Branching ratio estimate 61
5.5 Discussion on systematic uncertainties 61

Conclusions **65**

What next: KLOE-2 **67**

Bibliography **77**

Introduction

In 1918 Amalie Emmy Noether proved a theorem connecting the symmetries of the physical systems with the conservation laws [1], which became one of the greatest achievements of the twentieth century theoretical physics. It shows, for instance, that a system invariant under translations of time, space, or rotations will obey the laws of conservation of energy, linear momentum, or angular momentum, respectively. Since that time, symmetries have played a central role in almost all physics theories and models, especially in particle physics. As an example, every quantum field theory describing the interactions and the properties of elementary particles is formulated requiring Lorentz invariance. Furthermore, the discrete symmetries of parity $\mathcal{P}$, charge conjugation $\mathcal{C}$ and time reversal $\mathcal{T}$ proved to be very useful in the calculation of cross sections and decay rates, especially for those processes governed by strong interactions. These symmetries became central also in the formulation of the Standard Model.

Among the known elementary forces, the weak interaction has appeared to be very peculiar mainly because it violates $\mathcal{P}$ and $\mathcal{C}$ symmetries [2, 3], as well as their combination, $\mathcal{CP}$. The $\mathcal{CP}$ violation was discovered unexpectedly in 1964 by Christenson, Cronin, Fitch and Turlay while studying the regeneration of neutral K mesons [4]. In the framework of the Standard Model, the $\mathcal{CP}$ violation mechanism is introduced by the quark mixing described by the Cabibbo-Kobayashi-Maskawa matrix with one nonzero phase [5, 6], which requires the existence of three generation of quarks.

Parameters describing $\mathcal{CP}$ violation in the neutral kaon system were measured with a good precision by several experiments [7, 8], but there are still several open issues in which kaon physics can give a fundamental and unique contribution. Among these is the rare $K_{\mathrm{S}} \to \pi^+\pi^0\pi^-$ decay, whose decay amplitude receives contributions from a $\mathcal{CP}$-violating term and a $\mathcal{CP}$-conserving one. This is a kinematically suppressed decay and its branching ratio is $\sim 10^{-7}$. Despite three indirect measurements done by studying the K_L-K_S interference [9, 10, 11], this decay has never been observed directly and the KLOE Collaboration would likely perform the first direct measurement, exploiting the unique possibility of having pure K_S beams thanks to the tagging technique.

This thesis is focused on the direct measurement of the branching ratio of the $K_S \to \pi^+\pi^0\pi^-$ decay, based on ~ 1.7 fb^{-1} data set acquired by the KLOE experiment at the ϕ-factory DAΦNE at the Frascati National Laboratory of INFN. With a branching ratio of about 34%, the ϕ-meson decays to K_L-K_S final states, whose decay products are detected in the KLOE apparatus, consisting in a large-volume drift chamber and a lead-scintillating fiber electromagnetic calorimeter, both immersed in a 0.52 T axial magnetic field.

Since the momentum of the ϕ meson in the laboratory frame is small, kaon pairs are emitted almost back-to-back. Thus, their decay products are likely registered in opposite hemispheres of the apparatus. The detection of a K_L (K_S) meson in the apparatus ensures the presence of a K_S (K_L) with known momentum and direction (tagging technique). As normalization sample for the measurement, events in which the K_S presence is tagged by identifying the K_L interaction in the calorimeter will be used. Then, within this K_S-tagged sample, $K_S \to \pi^+\pi^0\pi^-$ decays are searched for by looking for their typical signature: two tracks of opposite curvature, given by the charged pions coming from a region close to the interaction point, and two energy deposits in the calorimeter by photons originating from $\pi^0 \to \gamma\gamma$ decays.

This thesis is divided into five chapters.

The $\mathcal{CP}$ violation in the neutral kaon system is briefly described for $K^0 \to \pi\pi$ and $K^0 \to \pi\pi\pi$ decays in chapter 1. Present measurements of the $K_S \to \pi^+\pi^0\pi^-$ decay are recalled as well.

The KLOE detector is described in chapter 2. A description of the drift chamber and the calorimeter is followed by a summary of the trigger system logic and the reconstruction of tracks, vertices and clusters.

In chapter 3 the data sample selection is presented. The method to tag K_S mesons is described, together with track and cluster selections for the signal topology search.

Chapter 4 describes data analysis and the strategy adopted to reject the background. The most relevant sources of background are from $\phi \to K^+K^-$ and

$K_S \to \pi^0\pi^0$ decays, which survive the selection of the signal and mimic the searched event topology.

In the last chapter the signal events extraction from data is presented, together with the estimation of the branching ratio of the $K_S \to \pi^+\pi^0\pi^-$ decay. Data are fit in the signal region using background and signal MC shapes, in order to simultaneously extract the number of signal events in data and the background normalization. Since this procedure relies upon MC simulations, the background normalization is evaluated in some control regions directly from data and compared to that given by the fit with signal as a cross-check. Furthermore, a fit without signal is also performed in the signal region to check if the signal hypothesis is favored instead. A stability check of the measured branching ratio is also reported in this chapter, together with a discussion of the systematic uncertainty which could affect the measurement.

This thesis presents the preliminary work done in preparation of the final measurement of the $K_S \to \pi^+\pi^0\pi^-$ decay. Present statistical uncertainty on the branching ratio measurement is 37%. Proposals for improving the analysis are reported and a plan on how to arrive to the final measurement is presented in the conclusions.

An additional last chapter points to future opportunities of measuring this rare decay at KLOE-2, the continuation of the KLOE experiment. KLOE-2 started its first data taking campaign in November 2014, acquired 2.4 fb^{-1} by December 2016 and just restarted its data taking with the aim of collecting more than 5 fb^{-1}. The additional statistics collected with the KLOE-2 experiment data taking campaign will increase by a factor of 3 the statistics used for the preliminary result presented in this thesis. Moreover the upgraded tracking system, with the presence of the Inner Tracker cylindrical-GEM detector, will allow to improve tracking and vertexing performance near the interaction region by a factor ~ 2 and, therefore, also background rejection capabilities. The measurement of the rare decay $K_S \to \pi^+\pi^0\pi^-$ will definitely profit from this detector upgrade. Nevertheless, since tracking and vertexing performance of this detector are being estimated using KLOE-2 data, it is not possible, at present, to evaluate what is the actual improvement this detector will introduce in the measurement of the $K_S \to \pi^+\pi^0\pi^-$ decay.

Chapter 1

Neutral kaon decays and $\mathcal{CP}$-symmetry violation

Kaons were discovered in 1947 by Rochester and Butler while studying cosmic-ray particles interactions in a cloud chamber [12]. These new particles, produced in strong interactions, decayed with typical lifetimes of weak processes. A new quantum number [13], strangeness (S), was introduced in order to explain the behavior of these new hadrons, known as K mesons or kaons.

Kaons appear in $I = \frac{1}{2}$ isospin doublets: $(K^+,\, K^0)$ with $S = 1$ and $(\overline{K^0},\, K^-)$ with $S = -1$. They are produced in strong processes like:

$$\pi^+ p \to K^+ \overline{K^0} p, \quad \pi^- p \to K^0 \Lambda^0, \quad p\bar{p} \to K^- K^0 \pi^+, \quad p\bar{p} \to K^+ \overline{K^0} \pi^-,$$

in which kaons with opposite strangeness are produced for conservation of strangeness. In kaon decays, instead, strangeness is not conserved and, at first order, transitions with $|\Delta S| = 1$ are allowed as in $K^+ \to \mu^+ \nu_\mu$ and $K^+ \to \pi^0 e^+ \nu_e$. Decays to fully-hadronic final states are also possible, such as $K^0(\overline{K^0}) \to 2\pi$ and $K^0(\overline{K^0}) \to 3\pi$. The violation of strangeness conservation in weak interactions lead Gell-Mann and Pais [14] to conclude, in 1955, that neutral kaons may transform one into another via second-order $|\Delta S| = 2$ processes like:

$$K^0 \to \pi\pi \to \overline{K^0} \quad \text{or} \quad K^0 \to \pi\pi\pi \to \overline{K^0},$$

whose quark diagrams are reported in fig. 1.1. Therefore, a kaon state with well defined mass and width can be treated as an admixture of K^0 and $\overline{K^0}$ during its time evolution [15].

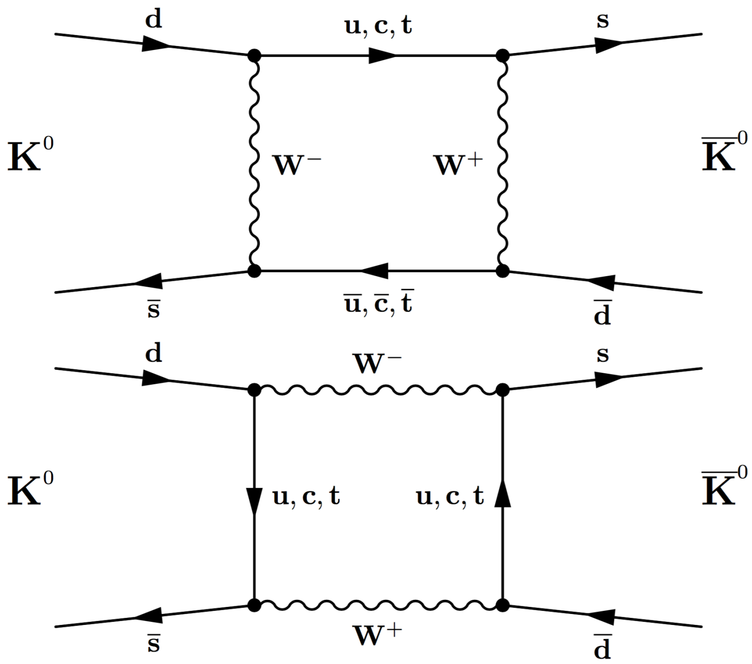

Figure 1.1: Quark diagrams for the $K^0 \leftrightarrow \overline{K^0}$ transitions

When, in 1957, the non-invariance of charge conjugation, $\mathcal{C}$, time reversal, $\mathcal{T}$, and parity, $\mathcal{P}$, in weak processes was introduced [16, 17, 18], Landau [19] suggested that weak interactions were invariant under the combined $\mathcal{C}$ and $\mathcal{P}$ symmetries, $\mathcal{CP}$. It is possible to build two linear combinations of the two strong neutral-kaon eigenstates, which correspond to the particles which actually decay to the $\mathcal{CP}$-even and $\mathcal{CP}$-odd 2π and 3π final states respectively[1]. Those true $\mathcal{CP}$ neutral kaons which decay weakly conserving $\mathcal{CP}$ are K_1 and K_2, defined as:

$$K_{1,2} = \frac{K^0 \pm \overline{K^0}}{\sqrt{2}}, \quad \text{with } \mathcal{CP} = \pm 1. \tag{1.1}$$

[1] $\mathcal{CP}\,|\pi^+\pi^-\rangle = +\,|\pi^+\pi^-\rangle$. $\mathcal{CP}\,|\pi^+\pi^0\pi^-\rangle = (-1)^{l+1}\,|\pi^+\pi^0\pi^-\rangle$, where l is the angular momentum of $\pi^+\pi^-$. Given the small available energy involved in the reaction ($m_{\mathrm{K}} - m_{3\pi} \simeq 90\,\mathrm{MeV}$), states with $l > 0$ are suppressed. Therefore $\mathcal{CP}\,|\pi^+\pi^0\pi^-\rangle = -\,|\pi^+\pi^0\pi^-\rangle$.

The $\mathcal{CP}$-even kaon has to decay to two pions, while the $\mathcal{CP}$-odd kaon has to decay to three pions in order to conserve the combined $\mathcal{CP}$ symmetry:

$$
\begin{aligned}
&K_1 \to \pi\pi && (\mathcal{CP} = +1),\\
&K_2 \to \pi\pi\pi && (\mathcal{CP} = -1).
\end{aligned}
$$

The lifetime of the $K_1 \to 2\pi$ decay is much shorter than the lifetime of the $K_2 \to 3\pi$ decay [20], because of the much larger available phase-space of the first decay:

$$
\begin{aligned}
\tau_1 \equiv \tau_{\mathrm{S}} &= (0.8954 \pm 0.0004) \times 10^{-10}\,\mathrm{s}\\
\tau_2 \equiv \tau_{\mathrm{L}} &= (5.116 \pm 0.021) \times 10^{-8}\,\mathrm{s}.
\end{aligned}
$$

This led to identify $K_1 \equiv K_{\mathrm{S}}$, the short-living neutral kaon, and $K_2 \equiv K_{\mathrm{L}}$, the long-living neutral kaon.

In 1964, it was observed that the K_{L} mesons decay to two charged pions with a branching ratio of $(2.0 \pm 0.4) \times 10^{-3}$ [4]. This experimental evidence lead to conclude that $\mathcal{CP}$ in not an exact symmetry of weak interactions and that K_{S} and K_{L} mesons are not pure $\mathcal{CP}$ eigenstates.

1.1 Neutral kaon mass eigenstates and $\mathcal{CP}$ symmetry

The time evolution of a neutral kaon system in the particle rest frame, in the $\left\{K^0, \overline{K^0}\right\}$ basis, is governed by the Hamiltonian $\mathbf{H}$ and the equation:

$$
i\frac{\partial}{\partial t}\begin{pmatrix} K^0 \\ \overline{K^0} \end{pmatrix} = \mathbf{H}\begin{pmatrix} K^0 \\ \overline{K^0} \end{pmatrix} = \left(\mathbf{M} - \frac{i}{2}\mathbf{\Gamma}\right)\begin{pmatrix} K^0 \\ \overline{K^0} \end{pmatrix}
$$

where $\mathbf{M}$ and $\mathbf{\Gamma}$ are 2×2 hermitian mass and decay matrices, the latter being responsible of the damping of the kaon wave-function in time[2]. In the Weisskopf-Wigner approximation, the elemets of the mass matrix $\mathbf{M}$ can be expressed as a

[2] The time-dependent factor of the wave-function is $\exp(-iEt) = \exp\left(-iMt - \frac{1}{2}\Gamma t\right)$, which is correct, provided that $\mathbf{\Gamma}$ has non-negative eigenvalues [21].

sum of strong and weak contributions [15]:

$$M_{ij} = m_K \delta_{ij} + \langle i| \mathbf{H_W} |j\rangle + \sum_{n \neq K^0, \overline{K^0}} \frac{\langle i| \mathbf{H_W} |n\rangle \langle n| \mathbf{H_W} |j\rangle}{m_K - E_n},$$

where m_K is the neutral kaon mass and $\mathbf{H_W}$ is the effective weak Hamiltonian. The sum $\sum_n |n\rangle \langle n|$ runs over all accessible states (both virtual and real) connecting K^0 and $\overline{K^0}$. The elements of the decay matrix $\mathbf{\Gamma}$ are related to the kaon decay width by unitarity and originate only from $\mathbf{H_W}$ [21]:

$$\Gamma_{ij} = 2\pi \sum_{n \neq K^0, \overline{K^0}} \delta(m_K - E_n) \langle i| \mathbf{H_W} |n\rangle \langle n| \mathbf{H_W} |j\rangle .$$

Without any assumptions on symmetry invariance, the Hamiltonian eigenstates of the neutral kaon can be written as [22]:

$$\begin{aligned} |K_\mathrm{S}\rangle &= \frac{1}{\sqrt{2(1+|\epsilon_S|)^2}} \left[(1+\epsilon_S)|K^0\rangle + (1-\epsilon_S)|\overline{K^0}\rangle\right] \\ |K_\mathrm{L}\rangle &= \frac{1}{\sqrt{2(1+|\epsilon_L|)^2}} \left[(1+\epsilon_L)|K^0\rangle - (1-\epsilon_L)|\overline{K^0}\rangle\right], \end{aligned} \tag{1.2}$$

where ϵ_S, ϵ_L are complex parameters accounting for possible $\mathcal{CP}$ and $\mathcal{CPT}$ violations. If $\mathcal{CPT}$ invariance holds, then $\epsilon_S = \epsilon_L = \epsilon$. If $\mathcal{CP}$ is an exact symmetry of weak interactions, then $\epsilon_S = \epsilon_L = 0$ and the mass eigenstates reduce to the $\mathcal{CP}$ eigenstates[3] in equation 1.1:

$$\begin{aligned} |K_\mathrm{S}\rangle &= \frac{1}{\sqrt{2}} \left[|K^0\rangle + |\overline{K^0}\rangle\right] \text{ with } \mathcal{CP} = +1 \\ |K_\mathrm{L}\rangle &= \frac{1}{\sqrt{2}} \left[|K^0\rangle - |\overline{K^0}\rangle\right] \text{ with } \mathcal{CP} = -1. \end{aligned} \tag{1.3}$$

1.2 $\mathcal{CP}$ violation in $K \to \pi\pi$ decays

When the $\mathcal{CP}$-violating decay $K_\mathrm{L} \to \pi^+\pi^-$ was observed in 1964, it was clear that $\mathcal{CP}$ was not an exact symmetry of weak interactions. Thus, the physical kaon states are not the $\mathcal{CP}$ eigenstates of eq. 1.3. However, the kaon states can still be

[3]The following phase convention is used: $\mathcal{CP}|K^0\rangle = |\overline{K^0}\rangle$ and $\mathcal{CP}|K^0\rangle = |\overline{K^0}\rangle$.

expressed in the $\{K_1, K_2\}$ basis:

$$
\begin{aligned}
|K_\mathrm{L}\rangle &= \frac{1}{\sqrt{1+|\epsilon|^2}} \left(|K_2\rangle + \epsilon\,|K_1\rangle\right) \\
|K_\mathrm{S}\rangle &= \frac{1}{\sqrt{1+|\epsilon|^2}} \left(|K_1\rangle - \epsilon\,|K_2\rangle\right)
\end{aligned}
\tag{1.4}
$$

Since there are no evidences for $\mathcal{CPT}$ violation, $\epsilon_S = \epsilon_L = \epsilon$ is assumed[4].

The $\mathcal{CP}$-symmetry breaking is explained by two distinct mechanisms, direct and indirect violations, the latter being due to the presence of the opposite-$\mathcal{CP}$ states in the kaon mass eigenstates. The direct violation occurs at vertices of weak decays and it is linked to the isospin of the decay final state, as can be understood by studying kaon decays to two pions. The 2π-system originating from kaon decays can have isospin $I = 0, 2$ (isospin equal to one is forbidden by Bose symmetry [29]) and can be written as:

$$
\begin{aligned}
|\pi^0\pi^0\rangle &= \sqrt{\frac{1}{3}}\,|\pi^0\pi^0; I=0\rangle - \sqrt{\frac{2}{3}}\,|\pi^0\pi^0; I=2\rangle \\
|\pi^+\pi^-\rangle &= \sqrt{\frac{2}{3}}\,|\pi^+\pi^-; I=0\rangle + \sqrt{\frac{1}{3}}\,|\pi^+\pi^-; I=2\rangle\,.
\end{aligned}
$$

The corresponding weak decay isospin amplitudes can be expressed as [21]:

$$
\begin{aligned}
\langle\pi\pi; I|\,\mathbf{H_W}\,|K^0\rangle &= \mathcal{A}_I e^{i\delta_I} \\
\langle\pi\pi; I|\,\mathbf{H_W}\,|\overline{K^0}\rangle &= \mathcal{A}_I^* e^{i\delta_I},
\end{aligned}
$$

where the isospin phase, δ_I, originating from strong interactions of pions, has been explicitly exhibited. The direct $\mathcal{CP}$ violation appears as a difference in the decay amplitudes of the kaon and the anti-kaon, which results in a phase difference between $\mathcal{A}_0$ and $\mathcal{A}_2$ [21]. This phase difference is generated by loop diagrams inducing $|\Delta I| = 3/2$ transitions, known as penguin diagrams, represented in fig. 1.2.

From the experimental point of view it is suitable to parametrize the direct $\mathcal{CP}$

[4]Although there are some theoretical prediction of $\mathcal{CPT}$ violation [23, 24, 25], all tests performed so far resulted in the confirmation that $\mathcal{CPT}$ symmetry is not broken [20, 26, 27, 28].

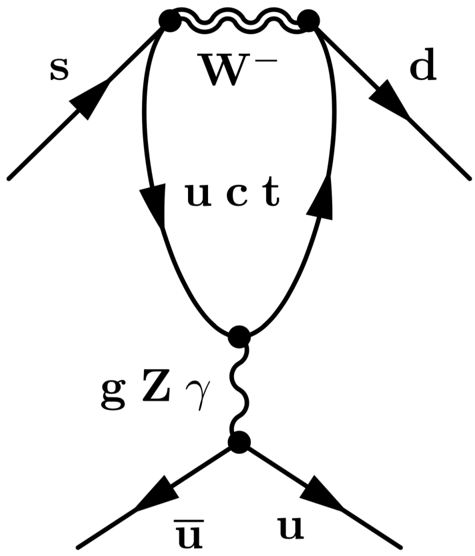

Figure 1.2: Example of penguin diagrams contributing to $K \to \pi\pi$ decays. The loop with W-boson exchange makes the s-quark change its flavor. The gluon exchange accounts for the QCD contribution to the decay, while the γ/Z^0 exchange accounts for electroweak contributions.

violation in $K \to 2\pi$ decays using the following observables [15]:

$$\begin{aligned}
\eta_{+-} &= \frac{\mathcal{A}(K_{\mathrm{L}} \to \pi^+\pi^-)}{\mathcal{A}(K_{\mathrm{S}} \to \pi^+\pi^-)} = |\eta_{+-}|e^{\phi_{+-}} \simeq \epsilon + \epsilon' \\
\eta_{00} &= \frac{\mathcal{A}(K_{\mathrm{L}} \to \pi^0\pi^0)}{\mathcal{A}(K_{\mathrm{S}} \to \pi^0\pi^0)} = |\eta_{00}|e^{\phi_{00}} \simeq \epsilon - 2\epsilon',
\end{aligned} \tag{1.5}$$

where ϵ is the mixing parameter introduced in eq. 1.4 and ϵ' accounts for direct $\mathcal{CP}$ violation. A convenient definition of ϵ' is [21]:

$$\begin{aligned}
\epsilon' &= \frac{\langle\pi\pi;0|\,\mathbf{H_W}\,|K_{\mathrm{S}}\rangle\,\langle\pi\pi;2|\,\mathbf{H_W}\,|K_{\mathrm{L}}\rangle - \langle\pi\pi;0|\,\mathbf{H_W}\,|K_{\mathrm{L}}\rangle\,\langle\pi\pi;2|\,\mathbf{H_W}\,|K_{\mathrm{S}}\rangle}{\sqrt{2}\,\langle\pi\pi;0|\,\mathbf{H_W}\,|K_{\mathrm{S}}\rangle^2} \\
&\simeq i\frac{e^{i(\delta_2-\delta_0)}\omega}{\sqrt{2}}\left(\frac{\Im\mathcal{A}_2}{\Re\mathcal{A}_2} - \frac{\Im\mathcal{A}_0}{\Re\mathcal{A}_0}\right),
\end{aligned}$$

where $\omega = \Re\mathcal{A}_2/\Re\mathcal{A}_0 \ll 1$ as a consequence of the $|\Delta S| = 1/2$ enhancement in kaon decays. A non-zero value of ϵ' is an unambiguous indication of direct $\mathcal{CP}$ violation.

Starting from the measurement of the ratio between $|\eta_{00}|$ and $|\eta_{+-}|$ it is possible to evaluate the strength of ϵ' using the formula [21]:

$$\Re\left(\frac{\epsilon'}{\epsilon}\right) \simeq \frac{1}{6}\left(1 - \frac{|\eta_{00}|^2}{|\eta_{+-}|^2}\right).$$

Above defined quantities have been measured with a good precision and values known today lead to conclude that $\mathcal{CP}$-symmetry is violated for a small amount [20].

$$\begin{aligned} |\eta_{+-}| &= (2.232 \pm 0.011) \times 10^{-3} & \phi_{+-} &= (43.51 \pm 0.05)^\circ \\ |\eta_{00}| &= (2.220 \pm 0.011) \times 10^{-3} & \phi_{00} &= (43.52 \pm 0.05)^\circ \\ |\epsilon| &= (2.228 \pm 0.011) \times 10^{-3} & \phi_{\epsilon} &= (43.52 \pm 0.05)^\circ \\ \Re\left(\frac{\epsilon'}{\epsilon}\right) &= (1.66 \pm 0.23) \times 10^{-3} & \mathrm{Arg}\left(\frac{\epsilon'}{\epsilon}\right) &= (-0.002 \pm 0.005)^\circ \end{aligned}$$

The quantity $\mathrm{Arg}\left(\frac{\epsilon'}{\epsilon}\right)$ is related to the possible $\mathcal{CPT}$-violating part of ϵ'/ϵ [21] and its value is in agreement with the statement that $\mathcal{CPT}$-symmetry does not break.

1.3 $\mathcal{CP}$ violation in $K \to \pi\pi\pi$ decays

$\mathcal{CP}$-symmetry violation may be observed also in three-pion decays of neutral kaons: the $\pi^+\pi^0\pi^-$ decay of the K_S is not forbidden by $\mathcal{CP}$ conservation, while the $\pi^0\pi^0\pi^0$ decay of the K_S is altogether $\mathcal{CP}$ violating [21], as can be derived by isospin considerations.

A three-pion system can be found in isospin states $I_{\pi\pi\pi} = 0, 1, 2, 3$, with third isospin component $I^{(3)}_{\pi\pi\pi} = 0$. The $|\Delta I| = 1/2$ rule disfavours $I_{\pi\pi\pi} = 2, 3$, energy-momentum conservation disfavours $\ell \neq 0$ angular momentum values. In fact, since the kaon mass and the three-pion state mass values are close, $\ell > 1$ values are suppressed. Since $\mathcal{CP}(\pi\pi\pi) = (-1)^I = (-1)^{\ell+1}$, where $\ell = \ell_{12}$, one obtains that $\mathcal{CP}(\pi^0\pi^0\pi^0) = -1$ for the Bose-Einstein symmetry requiring even values of angular momentum for the state of three identical pions. Therefore, $K_S \to \pi^0\pi^0\pi^0$ is $\mathcal{CP}$-violating. Similarly, one can deduct that $K_S \to \pi^+\pi^0\pi^-$ is $\mathcal{CP}$-conserving for $I = 0, 2$ and $\ell = 1$, while it is $\mathcal{CP}$-violating for $I = 1, 3$ and $\ell = 0$.

As for $K \to \pi\pi$ decays (see eq. 1.5), $\mathcal{CP}$ violation for $K \to \pi\pi\pi$ can be parametrized in the form [21]:

$$\eta_{+-0} = \frac{\mathcal{A}(K_S \to \pi^+\pi^0\pi^-, I=1)}{\mathcal{A}(K_L \to \pi^+\pi^0\pi^-)} = \epsilon + \epsilon'_{+-0}$$

and accordingly for $K_S \to \pi^0\pi^0\pi^0$, with similar definitions of η_{000} and ϵ'_{000}. Though $\ell = 1$ decays are disfavoured, the $\mathcal{CP}$-conserving decay amplitude dominates for the $K_S \to \pi^+\pi^0\pi^-$ process assuming negligible direct $\mathcal{CP}$ violation:

$$\eta_{+-0} = \frac{\mathcal{A}(K_S \to \pi^+\pi^0\pi^-, I=1)}{\mathcal{A}(K_L \to \pi^+\pi^0\pi^-)} = \epsilon + \epsilon'_{+-0} \simeq \epsilon. \tag{1.6}$$

Moving to decay rates from eq. 1.6, it is possible to write:

$$\frac{\Gamma(K_S \to \pi^+\pi^0\pi^-)}{\Gamma(K_L \to \pi^+\pi^0\pi^-)} = \frac{\tau_L}{\tau_S}\frac{\mathscr{B}(K_S \to \pi^+\pi^0\pi^-)}{\mathscr{B}(K_L \to \pi^+\pi^0\pi^-)} = |\epsilon|^2,$$

where $\mathscr{B}(\cdot)$ denotes the branching ratio of the process in parenthesis. The branching ratio of the $\mathcal{CP}$-violating $K_S \to \pi^+\pi^0\pi^-$ decay, $\mathscr{B}^{viol}(K_S \to \pi^+\pi^0\pi^-)$, can be estimated from the previous formula to be:

$$\mathscr{B}^{viol}(K_S \to \pi^+\pi^0\pi^-) = \frac{\tau_S}{\tau_L}\mathscr{B}(K_L \to \pi^+\pi^0\pi^-)|\epsilon|^2 = 1.1 \times 10^{-9}, \tag{1.7}$$

On the other hand, theory predictions for the branching ratio of the $\mathcal{CP}$-conserving $K_S \to \pi^+\pi^0\pi^-$ decay, $\mathscr{B}^{cons}(K_S \to \pi^+\pi^0\pi^-)$, are two orders of magnitude larger than the violating decay: 2.1×10^{-7} [30], 3.9×10^{-7} [31], $(2.4 \pm 0.7) \times 10^{-7}$ [32]. Accordingly to eq. 1.7, the branching ratio of the purely $\mathcal{CP}$-violating $K_S \to \pi^0\pi^0\pi^0$ decay, $\mathscr{B}(K_S \to \pi^0\pi^0\pi^0)$, can be estimated to be:

$$\mathscr{B}(K_S \to \pi^0\pi^0\pi^0) = \frac{\tau_S}{\tau_L}\mathscr{B}(K_L \to \pi^0\pi^0\pi^0)|\epsilon|^2 = 1.7 \times 10^{-9},$$

This decay has never been observed and the present upper limit, set by the KLOE experiment, is $\mathscr{B}(K_S \to \pi^0\pi^0\pi^0) < 2.6 \times 10^{-8}$ 90% C.L. [33]. The branching ratio $\mathscr{B}^{cons}(K_S \to \pi^+\pi^0\pi^-)$ has been measured, instead, by three experiments from the analysis of the Dalitz plot of the interference of the $K_S \to \pi^+\pi^0\pi^-$ and $K_L \to \pi^+\pi^0\pi^-$ amplitudes, as will be discussed in the following section.

1.4 Dalitz plot analysis and current measurements of $\mathscr{B}^{cons}(K_\mathrm{S} \to \pi^+\pi^0\pi^-)$

Since both kaons and pions are spinless, all observables and therefore also information about the dynamics, are embedded in the Dalitz plot distribution.

Referring to the transition in the kaon rest frame:

$$K(p_K) \to \pi^{(0)}(p_0)\pi^{(1)}(p_1)\pi^{(2)}(p_2)$$

one can define three invariants:

$$s_j = (p_K - p_j)^2 = m_K^2 + m_j^2 - 2m_K E_j$$

with the constraint[5]:

$$\sum_j s_j = 3m_K^2 + \sum_j m_j^2 - 2m_K \sum_j E_j = m_K^2 + \sum_j m_j^2.$$

Thus, it is possible to define only two independent variables, which can be defined as:

$$X = \frac{\sqrt{3}(T_1 - T_2)}{Q}$$
$$Y = \frac{3T_0 - Q}{Q},$$

where T_j are the pion kinetic energies in the kaon rest frame and the Q-value is:

$$Q = T_0 + T_1 + T_2 = m_K - \sum_j m_j.$$

For the process $K^0 \to \pi^0\pi^+\pi^-$, the typical values of the quantities involved in the previous formulae are: $Q = 83.5$ MeV, $p_j^{(max)} = 115$ MeV and $T_j^{(max)} = 42$ MeV. All points inside the boundary region defined by momentum conservation in the (X, Y) plane are kinematically allowed and represents possible decay events.

The decay rate is obtained integrating the squared modulus of the decay ampli-

[5] In the kaon rest frame it holds that: $\sum_j p_j = 0$ and $\sum_j E_j = m_K$.

tude over the full Dalitz plot distribution. Since the maximum allowed pion kinetic energy in three-pion decays is rather small, the Dalitz plot distributions are commonly expanded in powers of the Dalitz variables X and Y [21]:

$$|\mathcal{A}(K \to \pi\pi\pi\ )|^2 \propto 1 + gY + jX + hY^2 + kX^2$$

where $j \neq 0$ actually implies $\mathcal{CP}$-symmetry violation.

Symmetries of the Dalitz plot and the isospin of the three-pion final states of the kaon decay are connected to each other. The decay amplitude $\mathcal{A}(K_\mathrm{S} \to \pi^+\pi^0\pi^-\ )$ can be separated into two contributions with different isospin values, as already discussed in section 1.3: the $I = 1$ process is symmetric in X, while the $I = 2$ process is proportional to X. Thus, the difference between the integrals computed over the ranges $X > 0$ and $X < 0$ is sensitive to the K_L-K_S interference of the $\mathcal{CP}$-conserving $I = 2$ amplitudes, while the integration over the whole Dalitz plot (a region symmetric in X) let one to isolate the $I = 1$ violating term. Profiting of this Dalitz plot symmetries, some experiments studied the $I = 2$ interference to measure the $\mathcal{CP}$-conserving $K_\mathrm{S} \to \pi^+\pi^0\pi^-$ decay, as reported hereafter.

The E621 experiment at the Proton Center beamline at Fermilab searched for the $\mathcal{CP}$-conserving decay $K_\mathrm{S} \to \pi^+\pi^0\pi^-$ by looking for the interference between K_L and K_S produced in the interaction of a 800 GeV/c proton beam with a target. They measured the amplitude ratio:

$$\rho_{+-0} = \frac{\mathcal{A}(K_\mathrm{S} \to \pi^+\pi^0\pi^-, I = 2)}{\mathcal{A}(K_\mathrm{S} \to \pi^+\pi^0\pi^-)}$$

which is related to the measurable time dependent charge asymmetry by the relation:

$$A(t) = \frac{N_{X>0}(t) - N_{X<0}(t)}{N_{X>0}(t) + N_{X<0}(t)} = \frac{2D|\rho_{+-0}|\cos{(\Delta mt + \phi_{+-0})}e^{-t/2\tau_S}}{e^{-t/\tau_L}},$$

where $A(t)$ is the asymmetry, $N_{X>0}(t)$ $(N_{X>0}(t))$ is the $\pi^+\pi^0\pi^-$ yield per unit interval at proper time t in the half of the Dalitz plot where $X > 0$ $(X < 0)$, D is the dilution factor at production, $D = \frac{K^0 - \overline{K^0}}{K^0 + \overline{K^0}}$, Δm is the K_L-K_S mass difference, τ_S (τ_L) is the K_S (K_L) lifetime and ϕ_{+-0} is the phase of ρ_{+-0}. Fitting the data with the above function, they extracted $|\rho_{+-0}|$, ϕ_{+-0} and $\mathscr{B}^{cons}(K_S \to \pi^+\pi^0\pi^-)$ [9]:

$$\begin{aligned}
|\rho_{+-0}| &= (+39^{+9}_{-6}(\text{stat}) \pm 5(\text{syst})) \times 10^{-3} \\
\phi_{+-0} &= (-9 \pm 18)^\circ \\
\mathscr{B}^{cons}(K_S \to \pi^+\pi^0\pi^-) &= (4.8^{+2.2}_{-1.6}(\text{stat}) \pm 1.1(\text{syst})) \times 10^{-7}.
\end{aligned}$$

The CPLEAR experiment at the Low Energy Antiproton Ring at CERN used low-energy K^0 and $\overline{K^0}$ produced in antiproton interaction with a hydrogen gas jet target in the reactions $p\bar{p} \to \overline{K^0}K^+\pi^-$, $p\bar{p} \to K^0K^-\pi^+$, which allowed to tag the kaon flavour event by event. Defining:

$$\begin{aligned}
\eta_{+-0} &= \frac{\int \mathcal{A}_L^* \mathcal{A}_S^{(CP-)}\, dX\, dY}{\int |\mathcal{A}_S|^2\, dX\, dY}, \\
\rho_{+-0} &= \frac{\int_{X>0} \mathcal{A}_L^* \mathcal{A}_S^{(CP+)}\, dX\, dY}{\int_{X>0} |\mathcal{A}_S|^2\, dX\, dY} \\
&= -\frac{\int_{X<0} \mathcal{A}_L^* \mathcal{A}_S^{(CP+)}\, dX\, dY}{\int_{X<0} |\mathcal{A}_S|^2\, dX\, dY},
\end{aligned}$$

and the time dependent asymmetries for K^0 and $\overline{K^0}$:

$$\begin{aligned}
A_{X>0}(t) &= \frac{\bar{N}_{X>0}(t) - N_{X>0}(t)}{\bar{N}_{X>0}(t) + N_{X>0}(t)}, \\
A_{X<0}(t) &= \frac{\bar{N}_{X<0}(t) - N_{X<0}(t)}{\bar{N}_{X<0}(t) + N_{X<0}(t)}, \\
A(t) &= \frac{\bar{N}(t) - N(t)}{\bar{N}(t) + N(t)},
\end{aligned}$$

they extracted the $\mathcal{CP}$-conserving parameters by using the relations:

$$\begin{aligned}
A(t) &= 2\Re\epsilon - 2e^{-\Delta\Gamma t/2}\left[\Re\eta_{+-0}\cos(\Delta m t) - \Im\eta_{+-0}\sin(\Delta m t)\right] \\
A_{X>0,X<0}(t) &= 2\Re\epsilon - 2e^{-\Delta\Gamma t/2}[\Re(\eta_{+-0} \pm \rho_{+-0})\cos(\Delta m t) + \\
&\quad - \Im(\eta_{+-0} \pm \rho_{+-0})\sin(\Delta m t)],
\end{aligned} \tag{1.8}$$

where t is the decay proper time, Δm is the K_L-K_S mass difference, $\Delta\Gamma$ is the K_L-K_S decay-width difference and ϵ is the mass-mixing $\mathcal{CP}$-violating parameter of eq. 1.6.

They reported these measurements [10]:

$$\begin{aligned}
\Re\rho_{+-0} &= (+28 \pm 7(\text{stat}) \pm 3(\text{syst})) \times 10^{-3} \\
\Im\rho_{+-0} &= (-10 \pm 8(\text{stat}) \pm 2(\text{syst})) \times 10^{-3} \\
\mathscr{B}^{cons}(K_S \to \pi^+\pi^0\pi^-) &= (2.5^{+1.3}_{-1.0}(\text{stat})^{+0.5}_{-0.6}(\text{syst})) \times 10^{-7}.
\end{aligned}$$

The NA48 experiment at CERN studied the decays of K_L and K_S mesons produced by the interaction of a primary 400 GeV/c proton beam on a target. With similar definitions of quantities as above, they managed to extract the $\mathcal{CP}$-conserving parameters and branching ratio [11]:

$$\begin{aligned}
\Re\rho_{+-0} &= (+38 \pm 8(\text{stat}) \pm 6(\text{syst})) \times 10^{-3} \\
\Im\rho_{+-0} &= (-13 \pm 5(\text{stat}) \pm 4(\text{syst})) \times 10^{-3} \\
\mathscr{B}^{cons}(K_S \to \pi^+\pi^0\pi^-) &= (4.7^{+2.2}_{-1.7}(\text{stat})^{+1.7}_{-1.5}(\text{syst})) \times 10^{-7}.
\end{aligned}$$

The branching ratio value of the conserving $K_S \to \pi^+\pi^0\pi^-$ decay reported by the Particle Data Group (PDG) [20] is:

$$\mathscr{B}^{cons}(K_S \to \pi^+\pi^0\pi^-) = (3.5^{+1.1}_{-0.9}) \times 10^{-7}. \tag{1.9}$$

and it is the average of the three measurements by E621, CPLEAR and NA48.

1.5 Motivations for the measurement of the rare decay $K_S \to \pi^+\pi^0\pi^-$

The $\mathcal{CP}$-symmetry violation is one of the most intriguing puzzles in particle physics and its understanding is fundamental to precisely determine $\mathcal{CP}$-symmetry parameters in the quark sector of the Standard Model. Accurate measurements of the Dalitz plot of three-pion decays of kaons in each individual channel would allow a stringent test of the theoretical description of the $\Delta S = 1$ non-leptonic weak interactions and probe the effective theories which are currently used to make predictions.

The possibility of studying the interference in the neutral kaon systems is a peculiar feature of ϕ-factories, such as DAΦNE. Pure beams of (almost) monochromatic K_L and K_S mesons are produced at this facility, from the ϕ-meson decays. The quantum interference of the correlated K_L and K_S mesons shows up in relative time asymmetries through which the conserving part of the $K_S \to \pi^+\pi^0\pi^-$ decays can be measured. As described in [21], a convenient observable is represented by the transition rate for the entangled $K^0\overline{K^0}$ initial state to decay into the final states $f_1 = \pi\ell\nu$ at proper time t_1 and $f_2 = \pi^+\pi^0\pi^-$ at proper time t_2. By defining the time dependent asymmetries in a similar way as described in the previous section, it is possibile to isolate the coefficient appearing in the isospin amplitude of the purely $|\Delta I| = 3/2$ $\mathcal{CP}$-conserving $K_S \to \pi^+\pi^0\pi^-$ transition and evaluate the re-scattering phases, which parametrize the pion final-state interactions contributing to this weak process.

An alternative way of measuring the $K_S \to \pi^+\pi^0\pi^-$ decay is to directly observe the K_S mesons decaying to the $\pi^+\pi^0\pi^-$ final state. This is possibile at DAΦNE with the data acquired by the KLOE experiment. Since K_L and K_S are correlated, K_S mesons can be tagged and one can directly measure the $\pi^+\pi^0\pi^-$ yield of the tagged K_S mesons. Although the $\mathcal{CP}$-conserving and $\mathcal{CP}$-violating contributions of the decay rate are not distinguished, this measurement is still important because η_{+-0} and η_{000} contribute to the phase of the mixing parameter ϵ via the Lavoura's relation [34]:

$$\Gamma_{12} = 2\pi \sum_f \mathscr{B}(K_S \to f) \left[1 - |\eta_f|^2 - 2\Im\eta_f\right], \quad f = \pi^+\pi^0\pi^-, \pi^0\pi^0\pi^0. \tag{1.10}$$

It is also worth to notice that this would be the first direct measurement of the branching ratio $\mathscr{B}(K_S \to \pi^+\pi^0\pi^-)$. Considering the available KLOE statistics of 2004-2005 (~ 1.7 fb^{-1}), about 60 events are expected to be detected with 10% efficiency, assuming the branching ratio reported in eq. 1.9. A preliminary study of this decay has been performed in this thesis: we demonstrated that this measurement is feasible at KLOE at the same level of accuracy of the available indirect mesurements. Furthermore, by using the whole data sample which is being acquired by the KLOE-2 experiment (up to 5 fb^{-1}), running at DAΦNE, we can improve the uncertainty on this measurement by a factor ~ 2.

Chapter 2

The KLOE experiment at DAΦNE

DAΦNE is the ϕ-factory of Laboratori Nazionali di Frascati of the Italian Institute of Nuclear Physics (INFN): it is a e^+e^- collider operating at around 1020 MeV, the ϕ-meson mass. The ϕ-meson mainly decays to neutral kaon pairs (34%) and charged kaon pairs (49%), $\rho\pi$ (15%) and $\eta\gamma$ (1.3%) [20]. The ϕ decay products are detected by the KLOE apparatus, conceived for studying descrete symmetries, measuring charged and neutral kaon decay parameters and investigating light hadrons properties.

A short description of the accelerating machine and of the KLOE experimental apparatus is reported in this chapter, together with a brief overview of the trigger and the offline software.

2.1 The DAΦNE collider

The DAΦNE e^+e^- collider is optimized to operate at the center-of-mass energy $\sqrt{s} = m_\phi \simeq 1019.45$ MeV [35]. The layout of the accelerating complex is shown in fig. 2.1.

The heart of the collider are two storage rings in which up to 120 bunches of electrons and positrons are stored. Each bunch collides with its counterpart once per turn, minimizing the mutual perturbations of colliding beams. Electrons are accelerated to final energy of about 510 MeV in the LINAC (see fig. 2.1), accumulated and cooled in the accumulator and transferred to a single bunch in the ring. Positrons are created in an intermediate station in the LINAC, where 250 MeV elec-

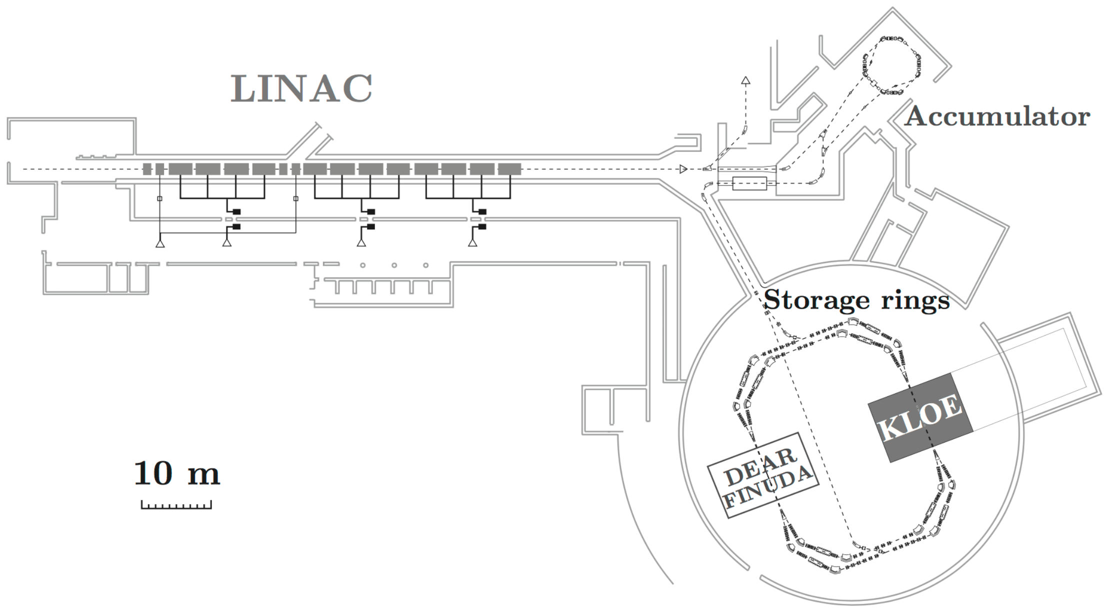

Figure 2.1: The DAΦNE complex schematic view.

trons hit a tungsten target to produce positrons. Positrons then follow the same processing as electrons in order to be injected in the main ring [35].

Electrons and positrons collide at an angle of $(\pi - 0.025)$ radians in the horizontal plane, with a frequency up to 356 MHz, corresponding to a bunch crossing period of $T_{\mathrm{rf}} = 2.7$ ns. The ϕ-meson thus moves in the laboratory frame with a momentum of about 13 MeV corresponding to $\beta_\phi \sim 0.015$, $\gamma_\phi \sim 1.0001$. Therefore, kaon beams from the ϕ decays are not monochromatic in the laboratory.

Neutral kaons have a momentum ranging between 104 and 116 MeV/c and it is a single valued function of the angle between the kaon momentum in the laboratory frame and the ϕ momentum, i.e. the x-axis[1]. The knowledge of the kaon direction to a few degrees allows to return to the ϕ center-of-mass, as can be seen in fig. 2.2. Charged kaons have an average momentum of 127 MeV/c [35].

[1]The coordinate system is defined such that the x-axis is in the horizontal plane, towards the center of DAΦNE , the y-axis is vertical, pointing upward, and the z-axis bisects the angle between the two beam lines.

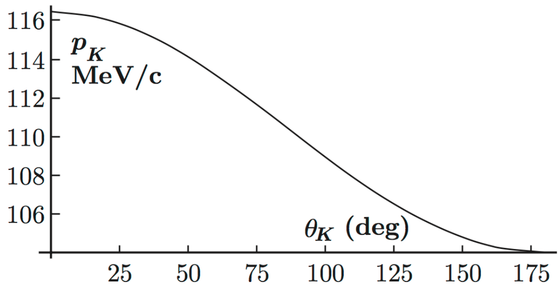

Figure 2.2: Laboratory momentum p_K as a function of the angle it forms with the x-axis for K^0-mesons.

2.2 The KLOE detector

The KLOE detector consists in a large cylindrical Drift Chamber, for reconstructing the trajectories of charged particles, and a hermetic Calorimeter, with a barrel and two end-cap modules, for measuring the energy and the entry point of photons. A superconducting coil and an iron yoke surrounding the calorimeter provides a 0.52 T axial magnetic field. The beam pipe at the interaction region (IR) is spherical in shape, with a 10 cm radius. It is made of a Beryllium-Aluminum alloy of 0.5 mm thickness. The sphere size is chosen to preserve the K_L-K_S interference.

The complexity of the apparatus (see fig. 2.3) is necessitated by the intent of KLOE to be a high-precision experiment. Its size is instead demanded by the long decay path of the K_L, 3.4 m. Thus, in order to capture approximately 40% of its decays, a detector with a core volume of a 2 meter radius is built.

2.2.1 The Drift Chamber

The KLOE Drift Chamber (DC) [36] is cylindrical in shape, with a length of 3.3 m and internal and external radii of 25 cm and 2 m, respectively. It is designed to register all charged secondary products from the K_L mesons decay and measure their properties with high precision. To minimize the K_L regeneration, the Coulomb multiple-scattering and the photon absorption, KLOE drift chamber is constructed out of carbon fiber composite with low-Z and low density and is filled with a gas mixture of helium (90%) and isobutane (10%). The radiation length of the gas amounts to about 900 m, including the contribution of the 52140 wires. Gold-plated tungsten wires are used as anodes; silver-plated aluminum wires have been chosen to

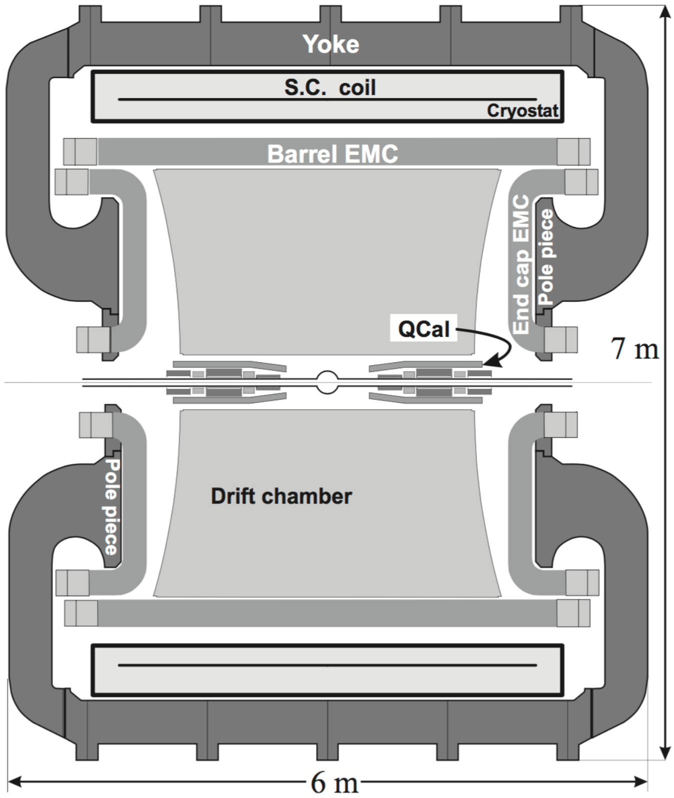

Figure 2.3: Vertical cross section of the KLOE detector, showing the interaction region, the drift chamber (DC), the electromagnetic calorimeter (EMC), the superconducting coil, and the return yoke of the magnet.

be field wires. The signals coming from sense wires are amplified, discriminated and transmitted to the read-out system: ADCs for dE/dx measurements and TDCs for time measurements. In order to obtain high and uniform track and vertex reconstruction efficiencies, wires are strung in an all-stereo geometry, with stereo angles varying with the radius of the chamber volume from 50 mrad to 120 mrad going outward. This design results in a uniform filling of the sensitive volume with almost square drift cells, with shape slowly changing along the z-axis. Particles from the ϕ decays are produced with small momenta and therefore track density is much higher at small radii. Thus, dimensions of the cells were designed to be of about 2×2 cm^2 for the 12 innermost wire layers and of about 3×3 cm^2 for the remaining 46 layers.

To extract the spatial position from the measured drift times of the incident particles, 232 space-to-time relations are used. They are parametrized in terms of two angles β and $\widetilde{\phi}$ defined in fig. 2.4. The β angle characterizes the geometry of the cell, directly related to the electric field responsible for the avalanche multiplication mechanism; $\widetilde{\phi}$ gives the orientation of the particle trajectory in the cell reference frame, defined in the transverse plane, with origin in the sense wire of the cell. Using the wire geometry, the space-to-time relations and the magnetic field, one can reconstruct the tracks and the vertices of charged particles.

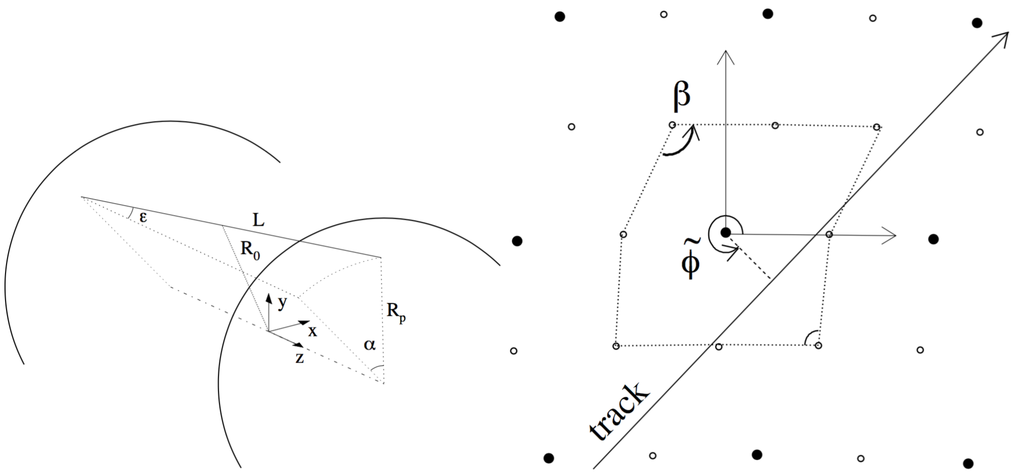

Figure 2.4: *Left*: wire geometry with the definition of the stereo angle ϵ between the wire of length L and the z-axis. *Right*: definition of β and $\widetilde{\phi}$ angles characterizing the shape of the cell and the angle of the incident track.

To ensure the stability in time of the KLOE drift chamber performance, the system is calibrated periodically by acquiring samples of cosmic-ray muon events, large enough for measuring more than 200 different space-to-time relations. The calibration is performed at the beginning of each KLOE run and selects about 8×10^4 cosmic-ray muon events. These events are tracked using the existing space-to-time relations and the average value of the residuals for hits in the central part of the cells is monitored. If these residuals exceed 40 μm, then additional 3×10^5 cosmic-ray muon events are collected, and a new set of calibration constants is provided.

The DC provides tracking in three dimensions with a resolution in the transverse plane of about 200 μm, a resolution along z of about 2 mm. The resolution on the decay vertex position is 1 mm for vertices inside the chamber volume and 3 mm for vertices reconstructed outside. The momentum of the particle is determined from the curvature of its trajectory in the magnetic field with a fractional accuracy $\sigma_p/p = 0.4\%$ for polar angles $45° < \theta < 135°$.

2.2.2 The Electromagnetic Calorimeter

The KLOE Electromagnetic Calorimeter (EMC) [37] is designed to provide hermetic detection of low energy photons with high efficiency, adequate energy resolution and excellent time resolution to reconstruct the vertex of K_{L} neutral decays. The calorimeter response has also to be fast since its signals are used to provide the main trigger of the events.

The calorimeter has a barrel module and two end-cap modules. The barrel calorimeter is a cylinder with inner diameter of 4 m, made of 24 trapezoidal modules, 4.3 m long and 23 cm thick. Each end-cap calorimeter consists in 32 vertical C-shaped modules. This structure ensures a coverage of 98% of the full solid angle. Each module consists of a mixture of lead (48% of the volume), scintillating fibers (42%) and epoxy (10%). Fibers, with a diameter of 1 mm each, are embedded in 0.5 mm lead foils to allow the showering processes. The special care in designing and assembling of the Pb-scintillating fiber composite ensures that the light propagates along the fiber in a single mode with velocity $\sim$ 17 cm/ns, which greatly reduces the spread of the arrival time of the light signals at the fiber ends. The calorimeter modules are read out at both sides by 4.4×4.4 cm^2 light guides coupled to photomultipliers, each defining a calorimeter cell. Signals from the photomultipliers are sent to ADCs for energy measurements and trigger, and to TDCs for time measurements. The calorimeter cells are then grouped to form five planes and twelve columns (see fig. 2.5).

When a particle hits the calorimeter, for each cell the charge and time the of arrival of the photomultiplier signals are registered. The amplitude of the signals, A_i, is proportional to the amount of the deposited energy, while the recorded times, t_i, are related to the time of flight of the particle. For each cell, the position of the readout elements and the difference of the arrival times at the two fiber ends determine the shower position with a 1 cm accuracy.

As a first step, the reconstruction program makes the average of time and energy of the recorded t_i and A_i for the two sides of each cell and compute the hit position. Corrections for attenuation length, energy scale, time offsets and light propagation speed are taken into account at this stage. A clustering procedure then groups together nearby clumps of energy deposition and calculates the average quantities over all the participating cells. The calibration constants to transform t_i and A_i

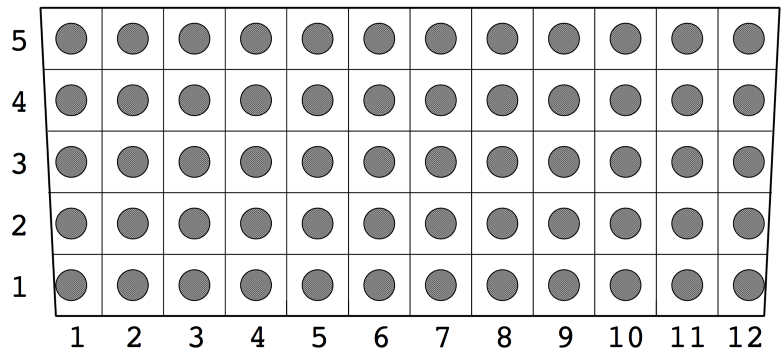

Figure 2.5: Schematic view of the Electromagnetic Calorimeter readout for the barrel module. There are 60 cells which defines 5 horizontal planes and 12 vertical columns. Filled dots represent photomultipliers.

from raw quantities to time in nanoseconds and energy in MeV are evaluated with dedicated online and offline algorithms.

The energy calibration starts by a first equalization in cell response to minimum ionizing particles (MIP) at calorimeter center and by determining the attenuation length of each single cell with a dedicated cosmic-ray trigger. This is done before the start of each long data taking period. The determination of the absolute energy scale in MeV relies instead on a monochromatic source of 510 MeV photons from $e^+e^- \to \gamma\gamma$ events. The determination of the linearity of the response is done with radiative-Bhabha scattering and $\phi \to \pi^+\pi^0\pi^-$ events. This last calibration is routinely carried out each 200-400 nb^{-1} of collected luminosity.

DAΦNE operates with a bunch-crossing period equal to the machine radio frequency (RF) period, $T_{\rm rf} = 2.715$ ns. Due to the spread of the particles arrival times, the trigger is not able to identify the bunch crossing related to each event, which has to be determined offline. The common start signal to the calorimeter TDC boards is provided by the first level trigger, which will be described in the next section. The stop is given, instead, by the photomultiplier signals delayed because of the electronics and light propagation in the fibers. The time associated to an energy cluster, $T_{\rm cl}$, is related to the time of flight of particles from the interaction point (IP) to the calorimeter, $T_{\rm tof}$, by the relation:

$$T_{\rm cl} = T_{\rm tof} + \delta_{\rm c} - N_{\rm bc}T_{\rm rf},$$

where $\delta_{\rm c}$ is a single number accounting for the overall electronic offsets and cable delays and N_{bc} is the number of bunch-crossing periods needed to generate the TDC start. The values of δ_{c} and N_{bc} are determined for each data taking run with $e^+e^- \to \gamma\gamma$ events by looking at the $T_{\mathrm{cl}} - R_{\mathrm{cl}}/c$ distribution, which exhibits well separated peaks corresponding to different values of N_{bc}. The constant δ_{c} is arbitrarily defined as the position of the peak with highest statistics, and T_{rf} is obtained from the distance between the peaks. Both quantities are evaluated with a precision better than 4 ps for a typical run of 200 nb^{-1} of integrated luminosity. This measurement of T_{rf} allows to set the absolute calorimeter time scale to better than 0.1%. During offline processing, to allow the cluster times to be related to the particle time of flight, δ_{c} is determined and, on an event by event basis, the global event start time $T_0 = N_{\mathrm{bc}}T_{\mathrm{rf}}$ is set, so that the corrected cluster time is obtained as follows:

$$t_{\mathrm{cl}} = T_{\mathrm{cl}} - (\delta_{\mathrm{c}} - T_0).$$

A starting value for all analyses is evaluated by assuming that the earliest cluster in the event is due to a photon originating at the interaction point. Further corrections are analysis dependent.

The high photon yield and the fine sampling enable cluster energies to be measured with a resolution of $\sigma(E)/E = 5.7\%/\sqrt{E\ (\mathrm{GeV})}$, as determined with the DC using Bhabha scattering events. The absolute time resolution $\sigma(t) = 57\ \mathrm{ps}/\sqrt{E\ (\mathrm{GeV})}$ is dominated by photoelectron statistics, which is well parametrized by the energy scaling law. A constant term of 140 ps has to be added in quadrature, as determined from $e^+e^- \to \gamma\gamma$, radiative ϕ decays and $\phi \to \pi^+\pi^-\pi^0$ data control samples. This constant term is shared between a channel-by-channel uncorrelated term and a common term to all channels. The uncorrelated term is mostly due to the calorimeter calibration while the common term is related to the uncertainty of the event T_0, arising from the DAΦNE bunch length and from the jitter in the trigger phase-locking to the machine RF. By measuring the average and the difference of $T_{\mathrm{cl}} - R_{\mathrm{cl}}/c$ for the two photons in $\phi \to \pi^+\pi^-\pi^0$, a similar contribution of about 100 ps for the two terms has been estimated.

Cluster position is measured with resolutions of 1.3 cm in the coordinate transverse to the fibers, and, by timing, of 1.2 cm$/\sqrt{E\ (\mathrm{GeV})}$ in the longitudinal coordinate. These performances enable the 2γ vertex in $K_{\mathrm{L}} \to \pi^+\pi^0\pi^-$ decays to be localized with a 2 cm resolution along the K_{L} line of flight, as reconstructed from the tagging K_S decay. Incidentally, the thin lead layers used and the high photon yield allow high reconstruction efficiency for low energy photons.

2.2.3 The trigger system

Event rates at DAΦNE, with a luminosity of 10^{32} cm^{-2}s^{-1}, amount to about 300 ϕ-mesons per second and 3×10^4 Bhabha scattering events per second within the KLOE acceptance.

The KLOE trigger system [38] is based on local energy deposits in the electromagnetic calorimeter and hit multiplicity information from the drift chamber. It has been optimized to retain almost all ϕ decays and provides efficient rejection on the two main sources of background: small angle Bhabha scattering events and particles lost from the DAΦNE beams, resulting in very high photon and electron fluxes in the interaction region. Moreover, all Bahbha scattering and $\gamma\gamma$ events produced at large polar angles are gathered for detector monitoring and calibration purposes, as well as comsic-ray muon events, which cross the detector at a rate of ~ 3 kHz.

Since the DAΦNE bunch crossing period amounts to $T_{\rm rf} = 2.7$ ns, the KLOE trigger must operate in continuous mode. A two level scheme has been chosen. A first level trigger, T1, is produced with a minimal delay of $\sim$ 200 ns and is synchronized with the DAΦNE master clock. The T1 signal initiates conversion in the front-end electronics modules, which are subsequently read out following a fixed time interval of about 2.6 μs, driven by the typical drift time of electrons in the drift chamber cells. After the arrival of a first level trigger, additional information is collected from the drift chamber, which is used together with the calorimeter information as a second level trigger, T2. It confirms the first level trigger, initializes digitisation of the drift chamber electronics and starts the data acquisition readout. If no T2 signal arrives before the end of 2.6 μs dead time, all readout is reset.

The T1 and T2 triggers are based on the topology of energy deposits in the KLOE electromagnetic calorimeter and on the number and spatial distribution of the drift chamber hits. Since ϕ decay events have a relatively high multiplicity, they can be efficiently selected by the calorimeter trigger by requiring two isolated energy deposits above a threshold of 50 MeV in the barrel and 150 MeV in the end-caps. Events with only two fired sectors in the same end-cap are rejected, because this topology is dominated by machine background. Moreover, 15 hits in the drift chamber within a time window of 250 ns from beam crossing are asked. The trigger identifies Bhabha scattering events requiring clusters with energy of about 350 MeV. An event which satisfies at least one of the two above mentioned conditions, and is not recognized as Bhabha event, generates the T1 signal[2]. The level-2 trigger, T2, requires further multiplicity or geometrical conditions for the energy deposits in the calorimeter, or about 120 drift chamber wire signals within a 1.2 μs time window. At this level, the trigger recognizes also cosmic-ray muon events by the presence of two energy deposits above 30 MeV in the outermost calorimeter layers. A fraction about 80% of the cosmic ray events are identified and rejected at the trigger level with this technique.

Further suppression of the DAΦNE background events and cosmic-ray particles is performed by the FILFO filter [39]. FILFO is an offline filter used to recognize and reject cosmic rays, machine background events and Bhabha scattering events with electrons (positrons) emitted with polar angles $\theta < 20°$ that interact with the low-beta focusing quadrupoles. To reject background events, cuts are applied on the number of clusters, the number of DC hits, the total energy deposited in the calorimeter, the position of the most energetic clusters, and the ratio of the number of hits in the internal DC layers to the total number of hits. A 1/20th sample of unfiltered data is used to control the filter efficiency.

For the search of the rare decay $K_S \to \pi^+\pi^0\pi^-$ both DC and EMC provide the trigger, as it is given by photons from the $\pi^0 \to \gamma\gamma$ decays or by the charged pions.

2.2.4 Data acquisition

The KLOE data acquisition (DAQ) [40] has been designed to cope with a rate of 10^4 events per second, due to ϕ decays, downscaled Bhabha events, non vetoed cosmic rays and DAΦNE machine background. An average event size of 5 kbytes is estimated, corresponding to a total bandwidth requirement of 50 Mbytes/s. The DAQ readout system involves some 23000 channels of front end electronics (FEE) from EMC, DC and trigger system. For each event, relevant data from the whole FEE system have to be concentrated in a single CPU where a dedicated process builds the complete event. A three level scheme has been implemented. The first

[2] As mentioned, part of the $e^+e^- \to e^+e^-$ events are gathered for detector monitoring and calibration.

level reads data from single FEE crates. The second level combines information from different crates. The last level, responsible for final event building, relies on standard network media and protocols (TCP/IP).

2.3 Data reconstruction

Data reconstruction starts immediately after the completion of the calibration jobs. The reconstruction program, DATAREC[39], provides additional data-quality and monitoring information, and consists of several modules, among which EMC reconstruction, DC reconstruction, track-to-cluster association and event-classification streaming procedure.

2.3.1 Cluster reconstruction

The calorimeter is segmented into 2440 cells, which are read out by photomultipliers (PMTs) at both ends (A, B). This segmentation provides the determination of the position of energy deposits in $r-\phi$ for the barrel and in $x-z$ for the end-caps. Both charges $Q^{\mathrm{A,B}}_{\mathrm{ADC}}$, from ADCs, and times $t^{\mathrm{A,B}}_{\mathrm{TDC}}$, from TDCs, are recorded. For each cell, the particle arrival time t and its coordinate s along the fiber direction (the zero being taken at the fiber center) are obtained using the times at the two ends as:

$$
\begin{aligned}
t(\mathrm{ns}) &= \frac{1}{2}(t^{\mathrm{A}} + t^{\mathrm{B}} - t_0^{\mathrm{A}} - t_0^{\mathrm{B}}) - \frac{L}{2v} \ , \\
s(\mathrm{cm}) &= \frac{v}{2}(t^{\mathrm{A}} - t^{\mathrm{B}} - t_0^{\mathrm{A}} + t_0^{\mathrm{B}}) \ ,
\end{aligned}
$$

with $t^{\mathrm{A,B}} = c^{\mathrm{A,B}} \times t^{\mathrm{A,B}}_{\mathrm{TDC}}$, where $c^{\mathrm{A,B}}$ are the TDC calibration constants, $t_0^{A,B}$ denotes overall time offsets, L stands for the length of the cell (cm) and v for the light velocity in fibers (cm/ns). The energy on each side of a cell i is obtained as:

$$
E_i^{\mathrm{A,B}}(\mathrm{MeV}) = k_E \times g_i(s) \times \frac{S_i^{\mathrm{A,B}}}{S_{i,\mathrm{MIP}}^{\mathrm{A,B}}} \ ,
$$

here $S = Q_{\mathrm{ADC}} - Q_{0,\mathrm{ADC}}$ is the charge collected after subtraction of the zero-offsets, the so-called ADC pedestals, and S_{MIP} is the response to a minimum ionizing particle crossing the calorimeter center. The correction factor $g(s)$ accounts for light attenuation as a function of the impact position s along the fiber, while k_E is the energy scale factor, obtained from showers of particles of known energy (see sec. 2.2.2). The cell energy E_i is taken as the mean of the energies at each end:

$$E_i(\mathrm{MeV}) = \frac{E_i^{\mathrm{A}} + E_i^{\mathrm{B}}}{2} \ .$$

The calorimeter reconstruction starts by applying the calibration constants to transform the measured quantities Q_{ADC} and t_{TDC} into the physical quantities S and t. Position reconstruction and energy/time corrections are applied to each fired cell. Then a clustering algorithm looks for groups of cells contiguous in $r-\phi$ or $x-z$ and groups them into pre-clusters. In a second step, the longitudinal coordinates and arrival times of the pre-clusters are used for further merging and/or splitting. The cluster energy, E_{cl}, is the sum of the energies of all cells assigned to a cluster. The cluster position, $(x, y, z)_{\mathrm{cl}}$, and time, t_{cl}, are evaluated as energy-weighted averages over the contributing cells. Cells are included in the cluster search only if times and amplitudes are available on both sides; otherwise, they are recorded as *incomplete* cells. The available information from most of the incomplete cells is added to the existing clusters at a later stage, by comparing the positions of such cells with the cluster centroid.

2.3.2 Track reconstruction

Track reconstruction is performed in three steps: pattern recognition, track fit, and vertex fit. Each step is managed separately and produces the inputs for the subsequent step.

Pattern recognition The pattern recognition algorithm searches for track candidates. It begins by associating hits, working inward from the outermost layer of the DC, and then obtains track segments and approximate trajectories parameters. The DC wires form alternating positive and negative stereo angles with respect to the z direction. When the hits are projected on the $x-y$ plane, they are seen in the stereo views as two distinct images. The pattern recognition procedure first associates separately the hits of each projection, using only two dimensional information, and in a second step combines the track candidates of the two views, according to their curvature values and geometrical compatibility.

Track fit The track-fit procedure minimizes the function $\chi^2_{\rm trk} = \sum_{i=1}^{n} (d_i - d_i^{fit})^2/\sigma_i^2$ defining the comparison between the measured and the expected drift distance for each hit. In this formula, n is the number of hits, $d_i(t_{\rm drift})$ is the drift distance, obtained via the space-to-time relation from the measured drift time (see sec. 2.2.1), d_i^{fit} is the result of the fit and σ_i is the estimate of the hit resolution. The procedure is iterative because the space-to-time relation depends on the track parameters. At each tracking step, the effects due to energy loss and multiple scattering are estimated.

Vertex fit The track parameters are used to look for primary and secondary vertices. For each track pair, a $\chi^2_{\rm vtx}$ function is computed from the distances of closest approach between tracks; the covariance matrices from the track-fit stage are used to evaluate the errors. The vertex position is obtained minimizing the $\chi^2_{\rm vtx}$.

2.3.3 Track-to-cluster association

The track-to-cluster association module makes correspondences between tracks in the DC and clusters in the EMC. The procedure starts by assembling the reconstructed tracks and vertices into decay chains and by isolating the tracks at the end of these chains. For each of these tracks, the measured momentum and the position of the last hit[3] in the DC are used to extrapolate the track to the EMC. The extrapolation gives the track length $L_{\bf ex}$ from the last hit in the chamber to the calorimeter surface, and the momentum $\vec{p}_{\bf ex}$ and the position $\vec{x}_{\bf ex}$ of the particle at the surface. The resulting impact point is then compared with the positions $\vec{x}_{\rm cl}$ of the reconstructed cluster centroids. A track is associated to a cluster if the distance to the centroid in the plane orthogonal to the direction of incidence of the particle on the calorimeter, $D = |(\vec{x}_{\rm cl} - \vec{x}_{\bf ex}) \cdot \vec{p}_{\bf ex}/|\vec{p}_{\bf ex}||$, is less than 60 cm.

[3]Conventionally, the last hit is defined as the track hit closest to the DC outer wall.

2.3.4 Event classification

At reconstruction level, data are divided into streams [41]. A stream is a collection of events which are all identified by a streaming algorithm. The streaming algorithms are implemented in such a way that they are not mutually exclusive, that is one event can be found in none, one or more than one stream.

The streaming procedure has been introduced in the KLOE event reconstruction in order to save CPU time and disk volume. In fact, among all the acquired events during the data taking, only part of them belongs to, e.g., the $\phi \to K_{\mathrm{L}}K_{\mathrm{S}}$ or $\phi \to \eta\gamma$ categories. Furthermore, by exploiting the streaming algorithms, users can select a definite stream for analysis purposes. For this thesis the interesting stream is $\phi \to K_{\mathrm{L}}K_{\mathrm{S}}$.

There are 7 streams defined:

- stream 1 (KPM): $\phi \to K^+K^-$;
- stream 2 (KSL): $\phi \to K_{\mathrm{L}}K_{\mathrm{S}}$;
- stream 3 (RPI): $\phi \to \rho\pi$, $\pi^+\pi^0\pi^-$;
- stream 4 (RAD): ϕ radiative decays, such as $\phi \to \eta\gamma$, $\phi \to \eta'\gamma$, $\phi \to \pi^0\gamma$;
- stream 5 (CLB): Bhabha and cosmic-ray muon events, to be used for calibration. This streams also contain $e^+e^- \to \mu^+\mu^-$ and $e^+e^- \to \pi^+\pi^-$ events;
- stream 6 (UFO): unidentified events;
- stream 7 (BHA): Bhabha scattering events.

The KSL stream has 8 sub-algorithms, each devoted to identify a special kaon decay and/or special event topologies. Among these algorithms, the KLCRASH has been chosen to identify K_{L} interactions in the calorimeter, through which K_{S} mesons are tagged, as described in next chapter.

2.4 Beam parameters and luminosity measurements

KLOE provides a continuous monitoring of the machine working point, providing feedback to DAΦNE continuously as well.

The most important parameters are the beam energies and crossing angle, which are obtained from the analysis of Bhabha scattering events with electron (positron) polar angles above 45°. The average value of the center-of-mass energy is evaluated online during data taking with a precision of $\sim$ 50 keV for each 200 nb^{-1} of integrated luminosity. This determination is further refined with offline analysis to achieve a precision of $\sim$ 20 keV, as discussed later. The average position of the e^+e^- primary vertex, with coordinates x_{PV}, y_{PV}, and z_{PV}, is reconstructed run-by-run from the same sample of Bhabha events. x_{PV} and y_{PV} are determined with typical accuracy of about 10 μm, and have widths Δx_{PV} and Δy_{PV} which are about 1 mm and few tens of microns, respectively. z_{PV} is also reconstructed online with 100-200 μm accuracy, but it has a natural width of 12-14 mm, determined by the bunch length [35].

An improved determination of the center-of-mass energy, $\sqrt{s}$, is obtained for each run by fitting the e^+e^- invariant-mass distribution for Bhabha events to a Monte Carlo generated function, which includes radiative effects and also initial and final state radiation corrections (ISR, FSR). The absolute energy scale is calibrated by measuring the visible cross section for the $\phi \to K_L K_S$ process. The cross section peak is fit to a theoretical function, which depends on the ϕ parameters, takes into account the effect of ISR, and includes the interference with the $\rho(770)$ and the $\omega(782)$ mesons. The ϕ mass, total width, and peak cross section are the only free parameters of the fit, $\rho(770)$ and the $\omega(782)$ parameters being fixed.

An online luminosity measurement is performed by selecting a sample of Bhabha scattering event within the acceptance of the barrel calorimeter, asking for two trigger sectors fired and using a high energy threshold. These selections allow to strongly reduce machine background and to provide DAΦNE with a luminosity estimation with only 3% statistical uncertainty, when operating at $L = 100\mu\text{b}^{-1}/\text{s}$ [35].

A more accurate measurement of the integrated luminosity is performed offline [42], by selecting Bhabha scattering events in polar-angle window $55° < \theta < 125°$, the so-called very large-angle Bhabha (VLAB) events. The effective cross section for these events, about 430 nb, is large enough to reduce the statistical error at a negligible level. The luminosity is obtained by counting the number of VLAB candidates, N_{VLAB}, and normalizing it to the effective Bhabha cross section, $\sigma^{\text{MC}}_{\text{VLAB}}$, obtained from MC simulation, after subtraction of the background, δ_{bkg}:

$$L_{\mathrm{int}} = \frac{N_{\mathrm{VLAB}}}{\sigma^{\mathrm{MC}}_{\mathrm{VLAB}}} (1 - \delta_{\mathrm{bkg}})$$

This method allows to estimate the luminosity with a 0.3% accuracy.

Chapter 3

Event selection

The data used in this analysis were collected with the KLOE apparatus in 2004-2005 at the center-of mass energy $\sqrt{s} \simeq m_\phi$. The total amount of data collected during this period amounts to about 1.7 fb^{-1}. Among all the acquired runs, we have chosen the ones with the most stable data taking conditions based on the experiment data quality.

3.1 Simulations of signal and background

The response of the KLOE detector is fully simulated for signal and background with the GEANFI software, based on GEANT3 [39]. For a given process, the momenta of the particles in the final state are generated according to the data taking conditions, and GEANFI simulates the detector response. Moreover, it allows to simulate the machine background on a run-by-run basis, i.e. simulation of accidental clusters and tracks follows the real data taking conditions, and the accidental activity is taken from $e^+e^- \to \gamma\gamma$ collinear events. The beam-induced background events are added to simulated events in the MC. The calorimeter clusters are simulated for all the particles as well, and also the DC hits for the charged particles. For the reconstruction of the events the same procedure applied to data (and explained in sec. 2.3) is used.

The background sample used for this analysis contains all ϕ decays to neutral and charged kaons, as well as radiative decays. Each decay is simulated with its branching ratio. An effective luminosity scale factor of 1.65 is applied to MC with respect to data.

A dedicated MC production has been used for K_S rare decays. Among these simulated rare decays, we select $K_S \to \pi^+\pi^0\pi^-$ decays for signal modeling. This decay is simulated with its branching ratio quoted by the PDG, 3.5×10^{-7}, with a luminosity scale factor of 30.

3.2 The K_S tag at KLOE

This analysis is devoted to the search of $\pi^+\pi^0\pi^-$ decays of the K_S mesons originating from $\phi \to K_L K_S$ decays. Since the ϕ-meson from e^+e^- collision at DAΦNE moves with a transverse momentum of about 13 MeV/c in the laboratory frame, K_L and K_S mesons, always produced in pairs in ϕ hadronic decays, are emitted almost back-to-back. Therefore, the detection of a K_L (K_S) with the apparatus ensures the presence of a K_S (K_L) in the other hemisphere, with a well defined momentum and direction. A sketch of the K_S tag through the identification of the K_L energy deposit in the calorimeter is shown in fig. 3.1: a large energy deposit is identified as a K_L crashing the calorimeter; thus, a K_S is tagged, which decays to $\pi^0\pi^0 \to 4\gamma$, as sketched in this picture.

Because of the exceptional timing capabilities of the EMC and the slowness of the kaons from ϕ decays, a time-of-flight-based technique is used to tag K_S mesons in a unique way. Neutral kaons have a velocity $\beta^* = 0.2162$ in the ϕ frame and β ranging from 0.193 to 0.239 in the laboratory and about 60% of K_L mesons reach the calorimeter in a time ≥ 31 ns. These K_L mesons interact in the calorimeter with an energy release up to their mass, 497 MeV. Hereafter, we define a K_L interaction in the EMC as K_L-crash, and we use it as a tag for the K_S.

For an energy release of 100 MeV we have a time resolution of about 0.3 ns, that is about a 2% accuracy on K_L velocity, shown in fig. 3.2. The above uncertainty on β^* translates into an accuracy on the kaon energy of ~ 0.25 MeV or ~ 1 MeV on its momentum with just one event.

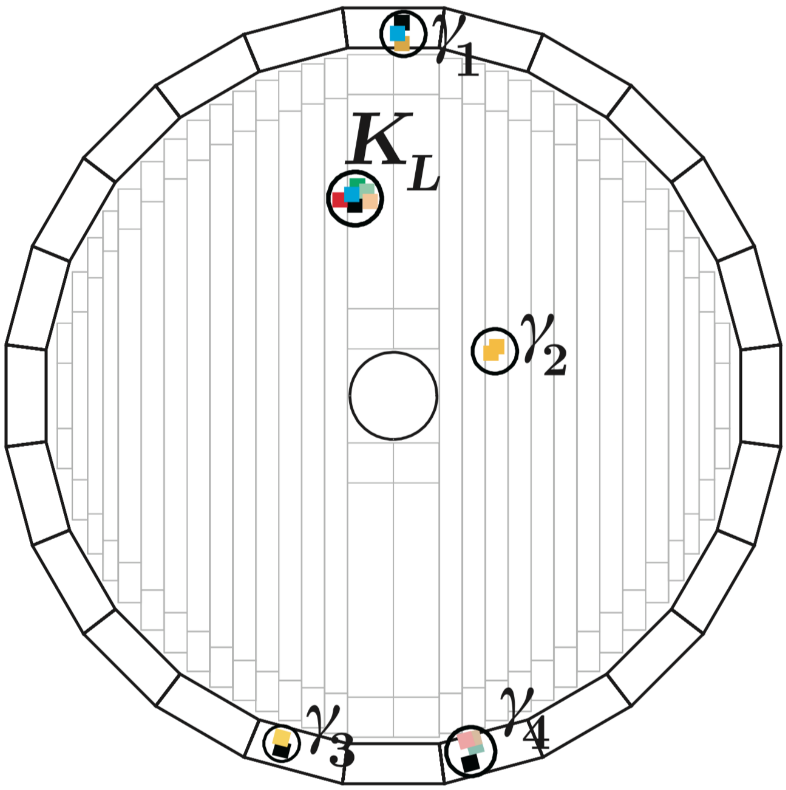

Figure 3.1: Sketch of the identification of K_S mesons by detecting the interaction of the K_L mesons in the calorimeter. The K_L literally crashes on the EMC releasing a large energy deposit. This allows to tag the K_S meson, which decays to $\pi^0\pi^0 \to 4\gamma$, indicated as $\gamma_1, \ldots, \gamma_4$ in this figure.

3.2.1 Identification of K_L-meson interactions in the calorimeter

The identification of K_L interactions in the calorimeter is performed after track and vertex reconstruction and after track-to-cluster association. As mentioned above, a K_L-crash is given by K_L mesons hitting the calorimeter, i.e. by K_L mesons not decaying within the drift chamber volume. A set of preselection cuts aims at rejecting, in fact, all the events in which a K_L decays in the DC volume. All events in which:

- two tracks with opposite curvature connected to a reconstructed vertex,
- two tracks with opposite curvature are connected to two vertices reconstructed less than 30 cm away from the interaction point in the transverse plane

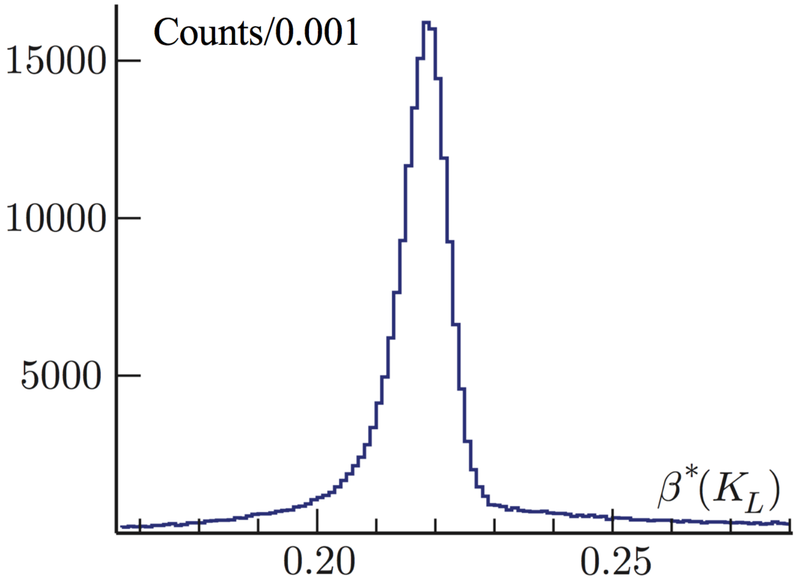

Figure 3.2: K_L velocity in the ϕ reference frame by time-of-flight measurement.

are discarded. These preselections largely reduce events coming from K_L decays, which may mimic a K_L-crash [43]. For each event passing these selections, we ask for clusters in the calorimeter which are not associated to tracks.

For each selected cluster, the velocity β_{cl} in the laboratory frame can be computed as:

$$\beta_{cl} = \frac{|\vec{R}_{cl}|}{c\,T_{cl}},$$

where $\vec{R}_{cl}$ denotes the cluster position with respect to the position of the e^+e^- interaction point (IP) and T_{cl} is the particle time of flight. Since the velocity of kaons in the ϕ rest frame is known, $\beta^* \simeq 0.2162$, it is convenient to transform β_{cl} to this reference frame:

$$\beta^* = \frac{\sqrt{\beta_{cl}^2 + \beta_\phi^2 + 2\beta_{cl}\beta_\phi\cos\alpha}}{1 + \beta_{cl}\beta_\phi\cos\alpha},$$

where $\beta_\phi \simeq 0.015$ is the ϕ boost in the laboratory frame and α is the angle between the ϕ boost and the vector connecting the interaction point to the cluster position. The distribution of β^* is shown if fig. 3.3a. The peak at ~ 1 mainly corresponds to cluster associated to photons from K_S decays close to the interaction point, while clusters originating from the residual K_L decays have $0.28 < \beta^* < 1$. The structure at around 0.22 corresponds, as expected, to K_L-crash in the calorimeter and the small excess at lower velocity values is due to charged particles, e.g. pions, for which the track-to-cluster association failed. These events are removed by selecting clusters with energy $E_{cr} > 100$ MeV. The same distribution after this cut is shown in fig. 3.3b. Therefore, clusters originating from K_L-crash in the calorimeter are selected asking for $0.17 < \beta^* < 0.28$ and $E_{cr} > 100$ MeV. The remaining background is due to cosmic-ray muons entering the apparatus which are not tracked by the drift chamber and to $\phi \to K^+K^-$ decay products.

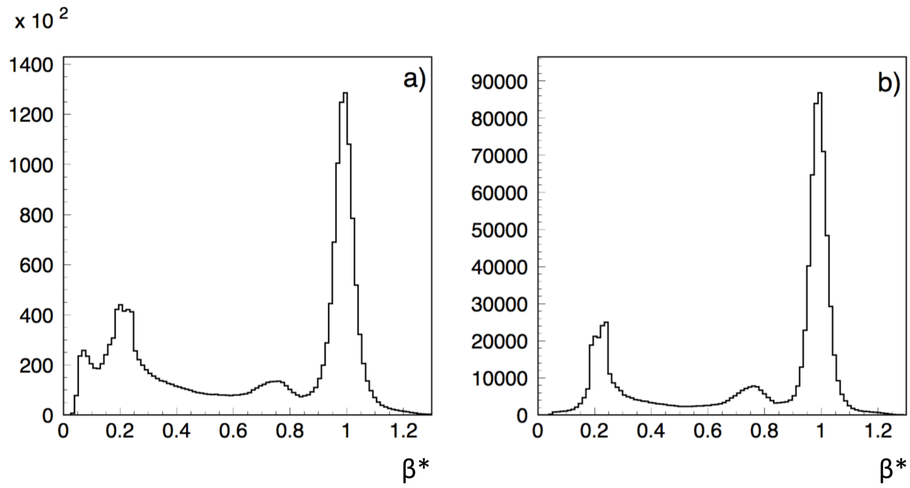

Figure 3.3: Neutral clusters velocity in the ϕ reference frame, before (a) and after (b) selecting clusters with energy $E_{cr} > 100$ MeV (see text).

Furthermore, kaons from ϕ decays are mostly emitted at large angles with respect to the beam axis, since the $K\bar{K}$ pair has the same angular momentum of the ϕ meson, $s = 1$. Thus, only events with clusters in the barrel calorimeter are retained.

To summarize, events with a K_L-crash are identified by asking for:

- clusters not associated to tracks;
- clusters releasing a energy deposit $E_{cr} > 100$ MeV only in the barrel;
- clusters with velocity $0.17 < \beta^* < 0.28$.

These selections for the tag have been extensively studied in previous KLOE analyses and the same values for the crash-cluster energy threshold and velocity have been exploited to select samples of K_S mesons for the analysis described in [33].

This analysis was devoted to set an upper limit on the branching ratio of the $\mathcal{CP}$-violating decay $K_S \to \pi^0\pi^0\pi^0$, whose final state contains six photons detected by the calorimeter. The spectra of E_{cr} and β^* for this six-photon sample are shown in fig. 3.4, left and right panels, respectively. As can be seen in this figure, the MC

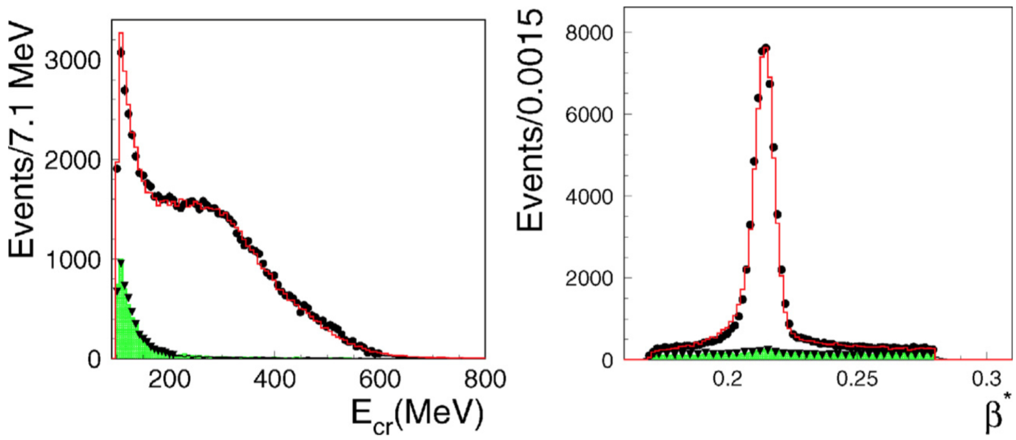

Figure 3.4: Distributions of the K_L energy deposit, left, in the EMC (E_{cr}) and the velocity, right, in the ϕ rest frame (β^*) for all events in the six-photon sample for the $K_S \to \pi^0\pi^0\pi^0$ decay (refer to [33]). Black points represent data, while the MC background simulation is shown as a red histogram. The same distributions for events rejected by the track veto are shown by the black triangles (data) and the green filled histograms (MC simulation).

simulation nicely reproduces the spectrum of the K_L-crash energy and of the velocity of all identified K_L mesons, after applying minor corrections to MC, as described in the same reference [33].

For the analysis described in this thesis, the same correction of E_{cr} has been implemented, while for β^* no corrections have been introduced.

The number of tagged K_S mesons observed in the whole data sample is:

$$N_{\mathrm{KS}}^{\mathrm{TAG}} = 5.26 \times 10^8,$$

with a tag efficiency estimated from the signal MC simulation of $\varepsilon_{\mathrm{tag}} = 0.3159 \pm 0.0037$. This efficiency value is in agreement with the tag efficiency measured also in previous KLOE analyses, based on K_L-crash [44]

3.2.2 K_L and K_S momentum estimate

By combining information about the K_L energy release and position in the calorimeter, the direction of its line of flight is determined with about 1° angular accuracy. Using the computed value of K_L four-momentum, $\mathbb{P}_\mathrm{L}$, and the run-average value of the ϕ-meson four-momentum as evaluated from Bhabha scattering events, $\mathbb{P}_\phi$, we determine the K_S four momentum from $\mathbb{P}_\mathrm{S} = \mathbb{P}_\phi - \mathbb{P}_\mathrm{L}$, with the same accuracy as for K_L.

In this analysis, the K_S-meson four-momentum derived from K_L-crash information is used to compute the K_S boost, $\vec{\beta}_\mathrm{S} = \vec{p}_\mathrm{S}/E_\mathrm{S}$, to perform the Lorentz transformation to move from the laboratory reference frame to the K_S reference frame when needed.

3.3 Considerations on background

One of the key points of this analysis is background rejection, since the expected signal yield is small. In Table 3.1 we have reported the decays which can be recognized as sources of background for the measurement of the rare decay $K_\mathrm{S} \to \pi^+\pi^0\pi^-$, together with the expected yield for each category, given an integrated luminosity of about 1 fb^{-1} and assuming a signal efficiency of 1. We have distinguished between prompt and delayed decays. The amount of expected signal events is reported for comparison. The numbers listed in Table 3.1 refer to a sample with no selections applied.

For our purposes, we have designated the following sources of background:

- $\phi \to K^+K^-$ decays;
- $\phi \to K_\mathrm{L}K_\mathrm{S}$, $K_\mathrm{S} \to \pi^0\pi^0$ decays;
- $\phi \to K_\mathrm{L}K_\mathrm{S}$, $K_\mathrm{S} \to \pi^+\pi^-(\gamma)$ decays;
- $\phi \to \pi^+\pi^0\pi^-$;
- *Other*: this category contains all prompt decays different from $\phi \to \pi^+\pi^0\pi^-$.

The prompt $\phi \to \pi^+\pi^0\pi^-$ and *Other* decays pass the tag requirements because an early accidental may mimic the K_L-crash and the final-state particles mimic the

Table 3.1: Background sources and corresponding expected events compared to signal events. 1000 signal events correspond to $\int Ldt \sim 1$ fb^{-1} and efficiency = 1.

	Source		Branching Fraction	events $\times 10^3$
delayed	$\phi \to K_L K_S$	$K_S \to \pi^+\pi^0\pi^-$	3.50 $\times 10^{-7}$	1
		$K_S \to \pi^0\pi^0$	1.05 $\times 10^{-1}$	300000
		$K_S \to \pi^+\pi^-(\gamma)$	2.37 $\times 10^{-1}$	677000
	$\phi \to K^+K^-$	$K^\pm \to \pi^0\pi^\pm$	2.02 $\times 10^{-1}$	577000
		$K^\pm \to \pi^0 e^\pm \nu$	4.96 $\times 10^{-2}$	142000
		$K^\pm \to \pi^0 \mu^\pm \nu$	3.28 $\times 10^{-2}$	94000
prompt	$\phi \to \pi^+\pi^0\pi^-$		1.53 $\times 10^{-1}$	437000
	$\phi \to \eta\gamma$	$\eta \to \pi^+\pi^0\pi^-$	3.00 $\times 10^{-3}$	8600
	$\phi \to \pi^0\gamma$	$\pi^0 \to e^+e^-\gamma$	1.52 $\times 10^{-5}$	43
	$\phi \to \pi^+\pi^-(\gamma)$		1.15 $\times 10^{-4}$	329
	$\phi \to \eta e^+e^-$	$\eta \to \gamma\gamma$	4.53 $\times 10^{-5}$	129
	$\phi \to \pi^0 e^+e^-$		1.12 $\times 10^{-5}$	32
	$\phi \to \omega\pi^0$	$\pi^+\pi^0\pi^-\pi^0$	4.2 $\times 10^{-5}$	130
		$\pi^0\gamma\pi^0$	3.9 $\times 10^{-6}$	12
		$\pi^+\pi^-\pi^0$	7.1 $\times 10^{-7}$	2

signal signature. The $\phi \to \pi^+\pi^0\pi^-$ and *Other* decays can be easily rejected with a cut on the invariant mass of the three pions with some other kinematical cuts, as will be described in next section. In $\phi \to K^+K^-$ decays, a charged kaon, or its decay products, may give a delayed signal in the calorimeter identified as a K_L-crash; the other charged kaon decay products mimic, instead, the K_S signal decay. In semileptonic decays, the two tracks are given by the lepton originating from the kaon which gives the crash and by the lepton originating from the other kaon decay. The genuine K_S tags with $K_S \to \pi^+\pi^-(\gamma)$ and $K_S \to \pi^0\pi^0$ also contribute as background, the latter mainly entering with $\pi^0 \to e^+e^-\gamma$ Dalitz decays or $\gamma \to e^+e^-$ conversions close to the interaction region. $K_S \to \pi^+\pi^-(\gamma)$ decays enter because of the presence of the two charged pions and a photon which couples to another photon from residual machine background.

Non-resonant processes, such as $e^+e^- \to \rho\gamma, \omega\pi^0, \omega\gamma$, have not been investigated as sources of background for this preliminary analysis, since these processes are not included in the MC simulation used for study the background. In these non-resonant processes an early particle may mimic the K_L-crash and the charged and neutral pions in the final state may mimic the signal signature. Dedicated simulations will be exploited in order to investigate such processes and a deep study will be performed for a more refined measurement.

3.4 Signal selection

In order to select $K_S \to \pi^+\pi^0\pi^-$ decays among all the tagged K_S mesons, a pre-selection is applied with the aim of selecting all decays with two neutral prompt clusters and two tracks connected to a reconstructed vertex close to the IP. This is, in fact, the signature of the decay under study: the two tracks are generated by the two charged pions and are reconstructed in the DC, while the two clusters are energy deposits in the EMC released by the two photons originating by the neutral pion decay, $\pi^0 \to \gamma\gamma$. Given the small K_S path legth, the position of the decay vertex is expected to be in a volume close to the IP. This topology is selected by asking for:

- 2 and only 2 *prompt* photons, i.e. clusters with energy $E_{\rm cl} > 7$ MeV and polar angle $|\cos\theta_{\rm cl}| < 0.915$, fulfilling $|t_{\rm cl} - R_{\rm cl}/c| < \min\{3.5\sigma_t, 2\text{ns}\}$, where $t_{\rm cl}$ is the cluster time measurement, $R_{\rm cl}$ is its reconstructed position and σ_t is the calorimeter time resolution (see sec. 2.2.2);

- 2 and only 2 tracks with opposite curvature, with their distance of closest approach (DCA) to the beam line such that $\rho_{\rm DCA} < 4$ cm and $|z_{\rm DCA}| < 10$ cm in the transverse and longitudinal projections, respectively. Furthermore, the first hit associated to each track must be less than 41 cm far from the DC center.

- a reconstructed vertex, connected to the two selected tracks, with position in a cylindrical volume surrounding the IP, defined as:

$$|\rho_{\rm VTX} - \rho_\phi| < 5 \text{ cm} \quad \text{and} \quad -7.5 \text{ cm} < |z_{\rm VTX} - z_\phi| < 8.5 \text{ cm},$$

  where $\rho_{\rm VTX} = \sqrt{x^2_{\rm VTX} + y^2_{\rm VTX}}$ and $z_{\rm VTX}$ are reconstructed taking into account the energy loss of the tracks passing through the beam pipe, the DC inner wall and gas-filled volume, while the average ϕ decay point is measured by large-angle Bhabha scattering events in each run.

These selections have been optimized to maximize signal efficiency and background rejection. Selecting more than two prompt photons does not improve the signal efficiency. The energy threshold for selecting photons set to 7 MeV, together with the $\theta_{\rm cl}$ range, allows to reject machine-induced background. Track and vertex selections are tuned to reject all background events in which particles decay within the DC volume or in the space between the DC inner wall and the beam pipe.

The number of events surviving the above pre-selections is reported in Table 3.2 for data, MC background and MC signal, normalized to data luminosity. The same

Table 3.2: Number of events after pre-selections normalized to data integrated luminosity.

	Data	K^+K^-	$\pi^+\pi^-(\gamma)$	$\pi^0\pi^0$	$\phi \to \pi^+\pi^0\pi^-$	*Other*	Signal
	3483015	1519997	1238388	182766	360126	182101	45
B/S		3.4×10^4	2.8×10^4	4.1×10^3	8.0×10^3	4.1×10^3	

Table also reports the background-to-signal ratios. The signal efficiency of pre-selections is $\varepsilon_{\rm pre} = 0.2622 \pm 0.0061$, as evaluated from the signal MC simulation. The main background sources for this analysis are $\phi \to K^+K^-$ decays, the most abundant, and the less copious $K_{\rm S} \to \pi^0\pi^0$ and *Other* decays. The strategy for background rejection will be described in next chapter.

Chapter 4

Data analysis

The relevant steps for background suppression will be described in this chapter. All the selection criteria presented in the following sections are intended to suppress background contribution to the data sample. This is a key point for this analysis in which the signal to be detected is small.

Present strategy is preparatory for a competitive measurement. Therefore, some ideas concerning the possible strategy to be adopted for a refined measurement will also be outlined.

4.1 Background rejection

In addition to the pre-selection described in sec. 3.4, the background rejection has been performed using some kinematical cuts, hereafter described. As already stated in the previous chapter, suppressing the background while enhancing signal is central for this analysis, since the signal we are searching for has a very small yield.

In order to reject background events, these steps are followed:

- $\pi^0 \to \gamma\gamma$ reconstruction is performed by means of a constrained fit, in order to improve the photon energy and, as a consequence, the $\pi^+\pi^0\pi^-$ system invariant mass and its direction;

- a cut on the K_L velocity in the ϕ-meson rest frame, β^*, is applied in order to reject a large fraction of background mainly due to $K_\mathrm{S} \to \pi^+\pi^-(\gamma)$ decays;

- apply a cut on the $\pi^+\pi^0\pi^-$ invariant mass, $M_{3\pi}$, to improve the signal to noise ratio for the main background sources;

4.1.1 $\pi^0 \to \gamma\gamma$ reconstruction

The resolution on the cluster energy measurement is not as good as the one on the track momentum. Therefore, in order to improve the π^0 reconstruction, we have built a kinematic fit of the $\pi^0 \to \gamma\gamma$ decay. The $\pi^0 \to \gamma\gamma$ reconstruction can be improved by exploiting the good time and position resolutions of the clusters in the calorimeter.

A fit with constraints is performed using the Lagrange multipliers method. The χ^2-like function to be minimized is:

$$\chi^2_{\pi^0} = \sum_{i=1}^{N_{\rm par}} \left(\frac{Y_{0,i} - Y_i}{\sigma_{0,i}} \right)^2 + \sum_{j=1}^{N_{\rm constr}} \lambda_j G_j ,$$

where $N_{\rm par} = 13$ is the number of parameters (assumed uncorrelated) and $N_{\rm constr} = 3$ is the number of constraints in the fit; $Y_{0,i}$ is the input parameter initial value with uncertainty $\sigma_{0,i}$; λ_j are the Lagrange multipliers and G_j are the constraints. For the $\pi^0 \to \gamma\gamma$ reconstruction we assume that the two photons originate from the two-track reconstructed vertex. We have used the following parameters:

- time, $t_{\gamma 1}$ and $t_{\gamma 2}$, of the two prompt clusters;
- energy, $E_{\gamma 1}$ and $E_{\gamma 2}$, of the two prompt clusters;
- position, $\vec{r}_{\gamma 1}$ and $\vec{r}_{\gamma 2}$, of the two prompt clusters;
- position, $\vec{r}_{\rm vtx}$, of the two-track reconstructed vertex.

Each parameter is varied at each stage of the minimization. The initial input parameters are the reconstructed values. The input resolutions, used also in previous KLOE analyses, are reported in Table 4.1. The three constraints to be fulfilled during the minimization are:

1. $|\vec{r}_{\gamma 1} - \vec{r}_{\rm vtx}| = ct_{\gamma 1}$;
2. $|\vec{r}_{\gamma 2} - \vec{r}_{\rm vtx}| = ct_{\gamma 2}$;

Table 4.1: Input resolutions for the $\pi^0 \to \gamma\gamma$ reconstruction.

σ_{t_γ}	$57\,\mathrm{ps}/\sqrt{E_\gamma\,(\mathrm{GeV})} \oplus 140\mathrm{ps}$
$\sigma_{E_\gamma}/E_\gamma$	$0.057/\sqrt{E_\gamma\,(\mathrm{GeV})}$
$\sigma_{xy,\gamma}$ (barrel), $\sigma_{xz,\gamma}$ (end-cap)	1.3 cm
$\sigma_{z,\gamma}$ (barrel), $\sigma_{y,\gamma}$ (end-cap)	$1.4\,\mathrm{cm}/\sqrt{E_\gamma\,(\mathrm{GeV})}$
$\sigma_{x,\mathrm{vtx}}$, $\sigma_{y,\mathrm{vtx}}$	1.1 cm
$\sigma_{z,\mathrm{vtx}}$	1.6 cm

3. $M_{\gamma\gamma} = m_{\pi^0}$, i.e. the two-photon invariant mass, $M_{\gamma\gamma}$, must be the π^0 mass, $m_{\pi^0} = 134.9766\,\mathrm{MeV}/c^2$ [20].

The output of this procedure are the fit χ^2 and:

- the improved time, $t_{\gamma 1}^{fit}$ and $t_{\gamma 2}^{fit}$, of the two prompt clusters;
- the improved energy, $E_{\gamma 1}^{fit}$ and $E_{\gamma 2}^{fit}$, of the two prompt clusters;
- the improved position, $\vec{r}_{\gamma 1}^{fit}$ and $\vec{r}_{\gamma 2}^{fit}$, of the two prompt clusters;
- the improved position, $\vec{r}_{\mathrm{vtx}}^{fit}$, of the two-track reconstructed vertex.

With these improved cluster energies and positions, and using also the improved vertex position, it is possible to compute the three-momentum of the photons. All the quantities whose calculation involves the photon four-momentum, e.g. $M_{3\pi}$ and the 3π-system direction, are improved by the fit, as a consequence of the π^0 reconstruction. Fig. 4.1 (left) shows the distribution of $\chi^2_{\pi^0}$ for data, together with the different backgrounds and the expected signal (magnified by a factor 10^4). The $\chi^2_{\pi^0}$ distribution for signal (magnified by a factor 10^4) is reported in the inset. The long tail in data and background distributions are due to events in which photons are wrongly paired to give a π^0. The MC signal spectrum is instead all contained in the region $\chi^2_{\pi^0} < 20$, as can be seen in the inset of fig. 4.1, in which this feature of the MC signal spectrum can be better appreciated.

The distribution of $M_{3\pi}$ is shown in fig. 4.1 (right) for MC signal using the reconstructed and the fit-improved photon energies: a good improvement is observed. The width of the distribution is about 5 MeV, to be compared to $\sim$ 20 MeV before the fit. Thanks to this improvement, this variable will be used for rejecting background, as will be described in sec. 4.1.3.

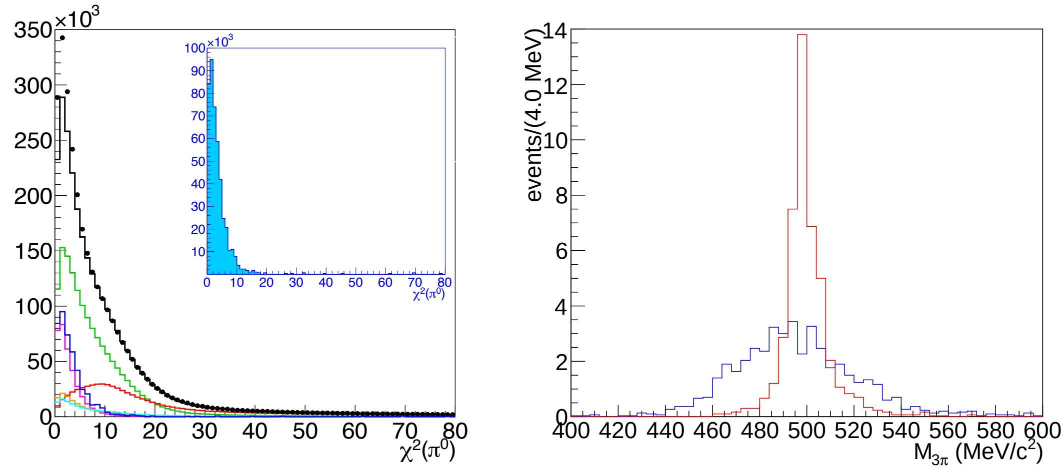

Figure 4.1: *Left*: Distribution of $\chi^2_{\pi^0}$ for data (black points), MC signal (blue histogram $\times 10^4$), MC total background (black histogram). The different colored histograms represent the background categories: $\phi \to K^+K^-$ (green), $K_S \to \pi^+\pi^-(\gamma)$ (red), $K_S \to \pi^0\pi^0$ (orange), $\phi \to \pi^+\pi^0\pi^-$ (magenta), *Other* (cyan). The $\chi^2_{\pi^0}$ distribution for signal (magnified by a factor 10^4) is reported in the inset. *Right*: Distribution of $M_{3\pi}$ for MC signal before (blue) and after (red) the π^0 reconstruction.

4.1.2 β^* acceptance window

After pre-selection, the number of events observed in data and the number of events predicted by MC for signal and background, listed in Table 3.2 in sec. 3.4, are reported in Table 4.2 to facilitate the reader.

Table 4.2: Number of events after pre-selections normalized to data integrated luminosity.

	Data	K^+K^-	$\pi^+\pi^-(\gamma)$	$\pi^0\pi^0$	$\phi \to \pi^+\pi^0\pi^-$	*Other*	Signal
	3483015	1519997	1238388	182766	360126	182101	45
B/S		3.4×10^4	2.8×10^4	4.1×10^3	8.0×10^3	4.1×10^3	

At this stage of the analysis, the distribution of β^* is shown in fig. 4.2 for data, together with MC backgrounds and the expected signal ($\times 10^4$). The distribution shows two peaks at $\beta^* = 0.215$ and 0.235, characteristic respectively of the $K_S \to \pi^0\pi^0$ and $K_S \to \pi^+\pi^-(\gamma)$ decays. This two-peak feature of the β^* distribution has always been observed in previous KLOE analyses, since it is due to the time synchronization of the experiment. The two peaks are separated by a β^* interval

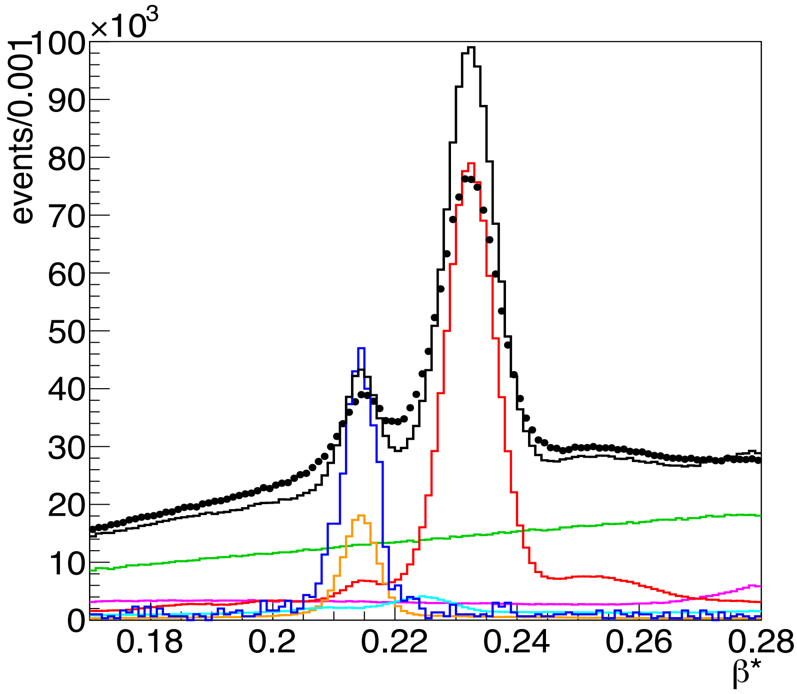

Figure 4.2: Distribution of β^* for data (black points), MC signal (blue histogram $\times 10^4$), MC total background (black histogram). The different colored histograms represent the background categories: $\phi \to K^+K^-$ (green), $K_S \to \pi^+\pi^-(\gamma)$ (red), $K_S \to \pi^0\pi^0$ (orange), $\phi \to \pi^+\pi^0\pi^-$ (magenta), *Other* (cyan).

corresponding to one bunch crossing, 2.7 ns, because the trigger signal is synchronized with the DAΦNE radio frequency. The trigger signal in each event is given by the two fastest particles, photons or pions, produced close to the interaction region and the e^+e^- collision time, T_0, is evaluated accordingly.

In a K_L-crash-selected sample, the tagged K_S mesons decay accordingly to their branching fractions and enter β^* regions depending on the reconstructed T_0. For $K_S \to \pi^0\pi^0$ the T_0 corresponds to the true collision time. For $K_S \to \pi^+\pi^-(\gamma)$, instead, the pion momentum range is 100-300 MeV and therefore most charged pions arrive to the calorimeter with a delay of up to 3 ns. Since the K_L time of flight to reach the calorimeter is about 30 ns, the velocity β^* of the K_L-crash clusters is overestimated by $\sim 10\%$ for $K_S \to \pi^+\pi^-(\gamma)$. The $\phi \to \pi^+\pi^0\pi^-$ and *Other* background events have a nearly uniform distribution of β^*, while the K^+K^- background is steadily increasing. The signal events are clustered around the value for $K_S \to \pi^0\pi^0$, since the trigger is likely to be produced by the two selected prompt photons.

By looking at fig. 4.2, it is clear that background can be suppressed requiring the K_{L}-crash velocity to be in the range:

$$0.205 < \beta^* < 0.225.$$

After this cut, the number of data and expected background and signal events are reported in Table 4.3, first raw; in the second raw the background-to-signal ratios, B/S, are listed for each background category.

Table 4.3: Number of events after the selection $0.205 < \beta^* < 0.225$, normalized to data integrated luminosity.

	Data	K^+K^-	$\pi^+\pi^-(\gamma)$	$\pi^0\pi^0$	$\phi \to \pi^+\pi^0\pi^-$	*Other*	Signal
	658281	260187	132416	139466	63230	52461	35
B/S		7.4×10^3	3.8×10^3	4.0×10^3	1.8×10^3	1.5×10^3	

The signal efficiency for this cut from MC simulation is $\varepsilon_{\beta^*} = 0.779 \pm 0.011$.

By selecting this narrower β^* window, systematic uncertainties could be introduced in the branching ratio measurement. By normalizing $K_{\mathrm{S}} \to \pi^+\pi^0\pi^-$ signal counts to $K_{\mathrm{S}} \to \pi^0\pi^0$ events in the same K_{L}-crash tagged sample could partially cancel this effect. In fact, the trigger timing and the β^* distributions of the two K_{S}-final states are very similar. This strategy in not presently applied to obtain the result presented in this thesis, but will be used for the final measurement. On the other hand, changing the β^* acceptance window will allow to estimate the contribution of this systematic error in the present study.

4.1.3 The three-pion invariant mass

Thanks to the kinematic-fit-improved π^0 reconstruction, the resolution on the $\pi^+\pi^0\pi^-$ invariant mass, $M_{3\pi}$, is improved, as shown in sec. 4.1.1. Therefore, we use this variable to reject background events which still pass the selection on β^*. The distribution of $M_{3\pi}$ for data, expected background and signal events ($\times 10^3$) is shown in fig. 4.3. We will retain all events fulfilling the following requirement:

$$480 < M_{3\pi} < 520\,\mathrm{MeV}/c^2.$$

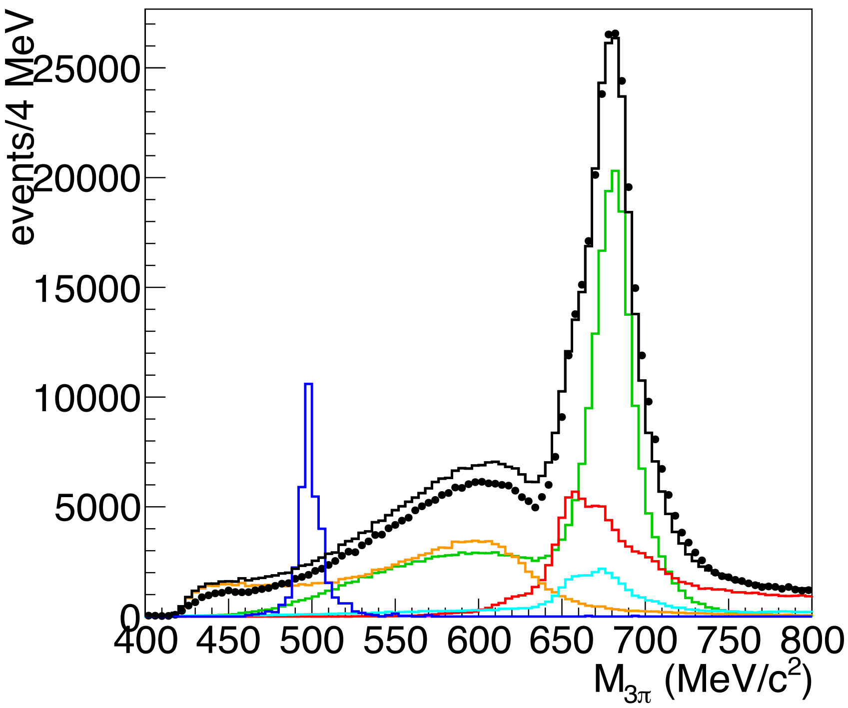

Figure 4.3: Distribution of $M_{3\pi}$ for data (black points), MC signal (blue histogram $\times 10^3$), MC total background (black histogram). The different colored histograms represent the background categories: $\phi \to K^+K^-$ (green), $K_S \to \pi^+\pi^-(\gamma)$ (red), $K_S \to \pi^0\pi^0$ (orange), $\phi \to \pi^+\pi^0\pi^-$ (magenta), *Other* (cyan).

The number of data, background and expected signal events after this additional cut are listed in Table 4.4, together with the B/S ratios for each background source. The signal efficiency for this cut from MC simulation is $\varepsilon_{M_{3\pi}} = 0.9314 \pm 0.0078$.

Table 4.4: Number of events after the selection $480 < M_{3\pi} < 520\,\mathrm{MeV}/c^2$, normalized to data integrated luminosity.

	Data	K^+K^-	$\pi^+\pi^-(\gamma)$	$\pi^0\pi^0$	$\phi \to \pi^+\pi^0\pi^-$	*Other*	Signal
	20346	9035	24	14989	13	1038	33
B/S		2.8×10^2	0.7	4.6×10^2	0.4	31.8	

4.2 Signal and control regions

By looking at the correlation between the angle formed by the K_L and the $\pi^+\pi^0\pi^-$ system, α_LS, and the angle formed by the two tracks at the origin in the K_S rest frame, $\alpha^*_{\pi\pi}$, it is possible to define a signal region (SBOX) and two control regions, each dominated by a specific background category. Fig. 4.4 shows the correlation $(\alpha_\mathrm{LS}, \alpha^*_{\pi\pi})$ for MC backgrounds and expected signal. Dalitz decays of the π^0 and photon conversions are expected to be clustered at small values of $\alpha^*_{\pi\pi}$, while the two-body decays $\pi^+\pi^-(\gamma)$ and K^+K^- are expected to be clustered close to 180°. Signal events are expected to be observed in the region of α_LS close to 180° . Fig. 4.5 shows the same correlation plot for data, where signal region and control regions are delimited by red lines and labeled with their names:

SBOX is the signal box, defined as:

$$80^\circ < \alpha^*_{\pi\pi} < 180^\circ \quad \vee \quad 150^\circ < \alpha_{LS} < 180^\circ\,;$$

CRKK is the control region with about 90% of $\phi \to K^+K^-$ decays, defined as:

$$130^\circ < \alpha^*_{\pi\pi} < 170^\circ \quad \vee \quad 0^\circ < \alpha_{LS} < 140^\circ\,;$$

CR2PI0 is the control region with about 96% of $K_\mathrm{S} \to \pi^0\pi^0$ decays, defined as:

$$0^\circ < \alpha^*_{\pi\pi} < 30^\circ \quad \vee \quad 90^\circ < \alpha_{LS} < 180^\circ\,.$$

Table 4.5 lists the data and MC events in the two control regions, while Table 4.6 reports the number of data, MC background and expected signal in the signal box, together with the background-to-signal ratios, B/S. The signal efficiency of the SBOX selection is $\varepsilon_\mathrm{SBOX} = 0.9151 \pm 0.0089$ as evaluated from MC simulation.

We exploit the selected control regions in order to study the normalization of the different background contributions. Two quantities have been chosen to check the data/MC agreement in these control regions:

1. the momentum of charged pions in the K_S rest frame, p^*_π;
2. the angle $\alpha_{\pi^0,\mathrm{miss}}$ formed by the direction of the kinematic-fit-improved π^0 and the direction of the K_L-2track system, that is the missing π^0.

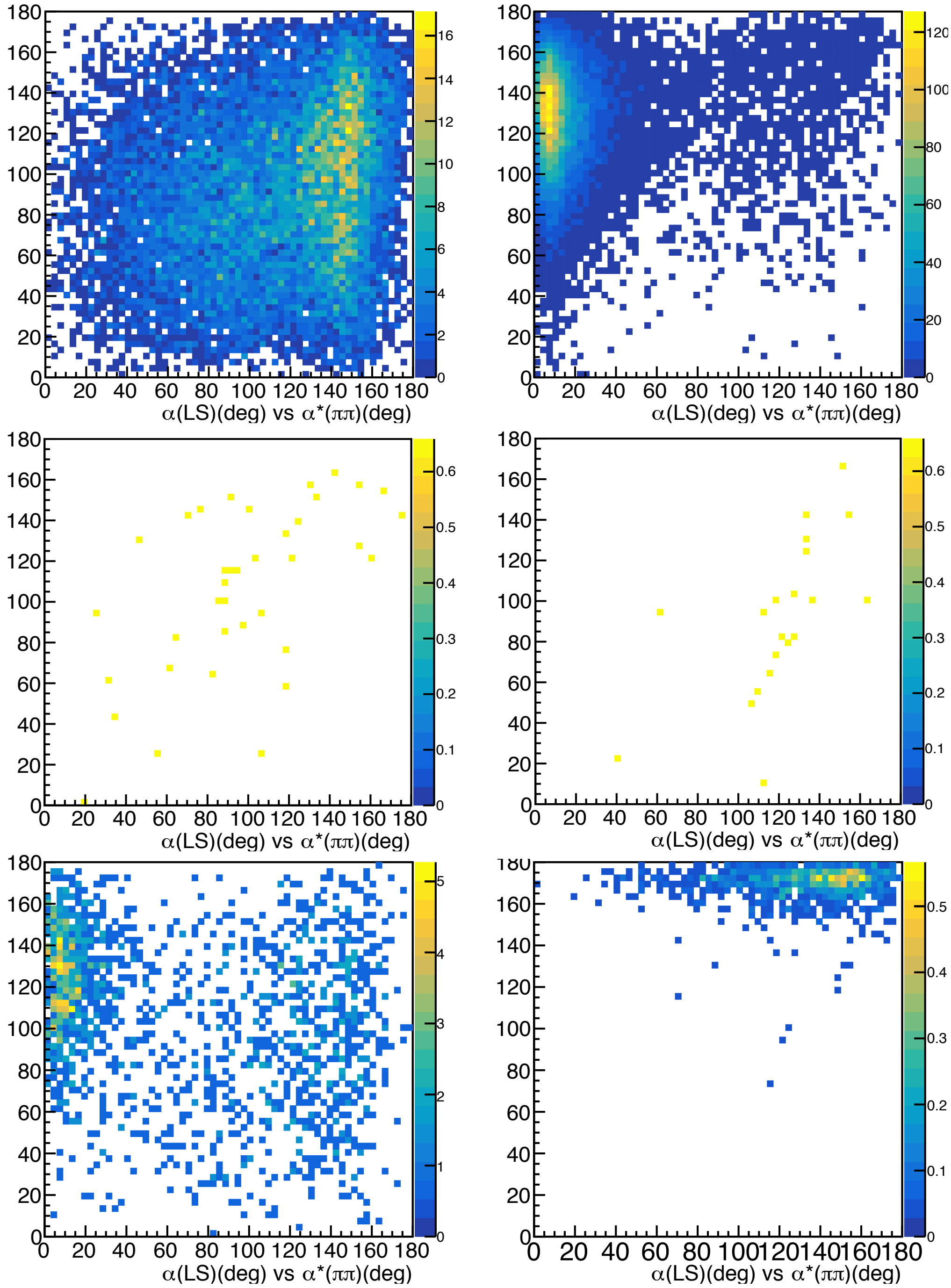

Figure 4.4: Correlation $(\alpha_{\rm LS}, \alpha^*_{\pi\pi})$ for MC backgrounds and expected signal. Top left: MC K^+K^-; top rigth: MC $\pi^0\pi^0$; center left: MC $\phi \to \pi^+\pi^0\pi^-$; center right: MC $\pi^+\pi^-(\gamma)$; Bottom left: MC *Other*; Bottom right: MC signal.

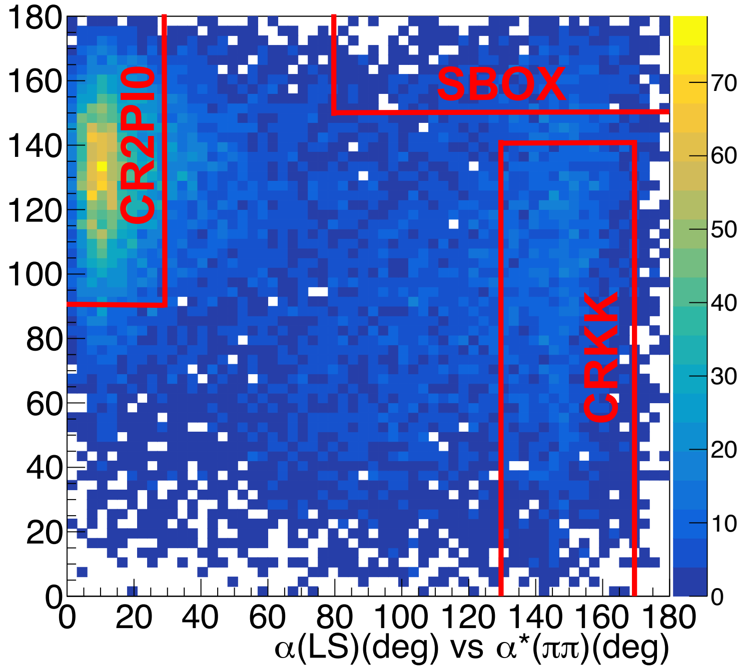

Figure 4.5: Correlation $(\alpha_{\mathrm{LS}}, \alpha_{\pi\pi})$ for data. Signal and control regions are delimited by red lines in the latter figure and labeled with their names: SBOX is the signal box, CRKK is the control region with about 89% of $\phi \to K^+K^-$ decays and CR2PI0 is the control region in which about 91% decays are $K_{\mathrm{S}} \to \pi^0\pi^0$.

3. the *track mass*, m^2_{TRK}, which requires the missing mass of the K_{L}-2track system to coincide with m_{π^0} when the two tracks have the same mass. This quantity is derived from the following relation:

$$\left(\sqrt{s} - E_{\mathrm{L}} - \sqrt{p_+^2 + m^2_{\mathrm{TRK}}} - \sqrt{p_-^2 + m^2_{\mathrm{TRK}}}\right)^2 - (\vec{p}_+ + \vec{p}_-)^2 = m^2_{\pi^0}\,,$$

where $\sqrt{s}$ is the center-of-mass energy, E_{L} is the K_{L} energy and $\vec{p}_k$ is the momentum vector of the opposite-curvature selected tracks.

These variables will also be used for extracting the number of signal events in data, as will be described in next section.

The distributions of p^*_π, $\alpha_{\pi^0,\mathrm{miss}}$ and m^2_{TRK} in the CRKK and CR2PI0 regions for data and predicted backgrounds are shown in fig. 4.6 and fig. 4.7. As can be seen from these figures, MC spectra nicely reproduce data distributions in CRKK after having applied the scaling factors, R^{CR}_j, defined as the ratio between data events

Table 4.5: Number of data and MC events in each control region defined in the text, normalized to data integrated luminosity.

	Data	K^+K^-	$\pi^+\pi^-(\gamma)$	$\pi^0\pi^0$	$\phi \to \pi^+\pi^0\pi^-$	*Other*	Signal
CRKK	3355	3205	1	182	3	190	0
CR2PI0	7259	121	1	11534	0	382	0

Table 4.6: Number of data, MC background and expected signal events in the signal region defined in the text, normalized to data integrated luminosity. The signal-to-background ratios are also reported for the SBOX selection for each background source.

	Data	K^+K^-	$\pi^+\pi^-(\gamma)$	$\pi^0\pi^0$	$\phi \to \pi^+\pi^0\pi^-$	*Other*	Signal
SBOX	1003	565	4	381	1	45	30
B/S		28.6	0.2	13.5	3.2×10^{-2}	2.3	

and MC events of category j in the corresponding control region:

$$R_j^{\mathrm{CR}} = N_{\mathrm{D}}/N_j^{\mathrm{CR}}\,.$$

The data/MC agreement in the CR2PI0 region, after correcting for the corresponding $\pi^0\pi^0$ scaling factor, is not at the same level of what observed in CRKK and will be better investigated for a refined analysis. The values obtained for the rescaling fators are:

$$R_{K^+K^-}^{\mathrm{CR}} = 1.047 \pm 0.026$$
$$R_{\pi^0\pi^0}^{\mathrm{CR}} = 0.6293 \pm 0.0094.$$

We expect the CRKK and CR2PI0 scaling factors evaluated in the control regions to be valid also in the signal box region after estimating the abundance of each j-th background component.

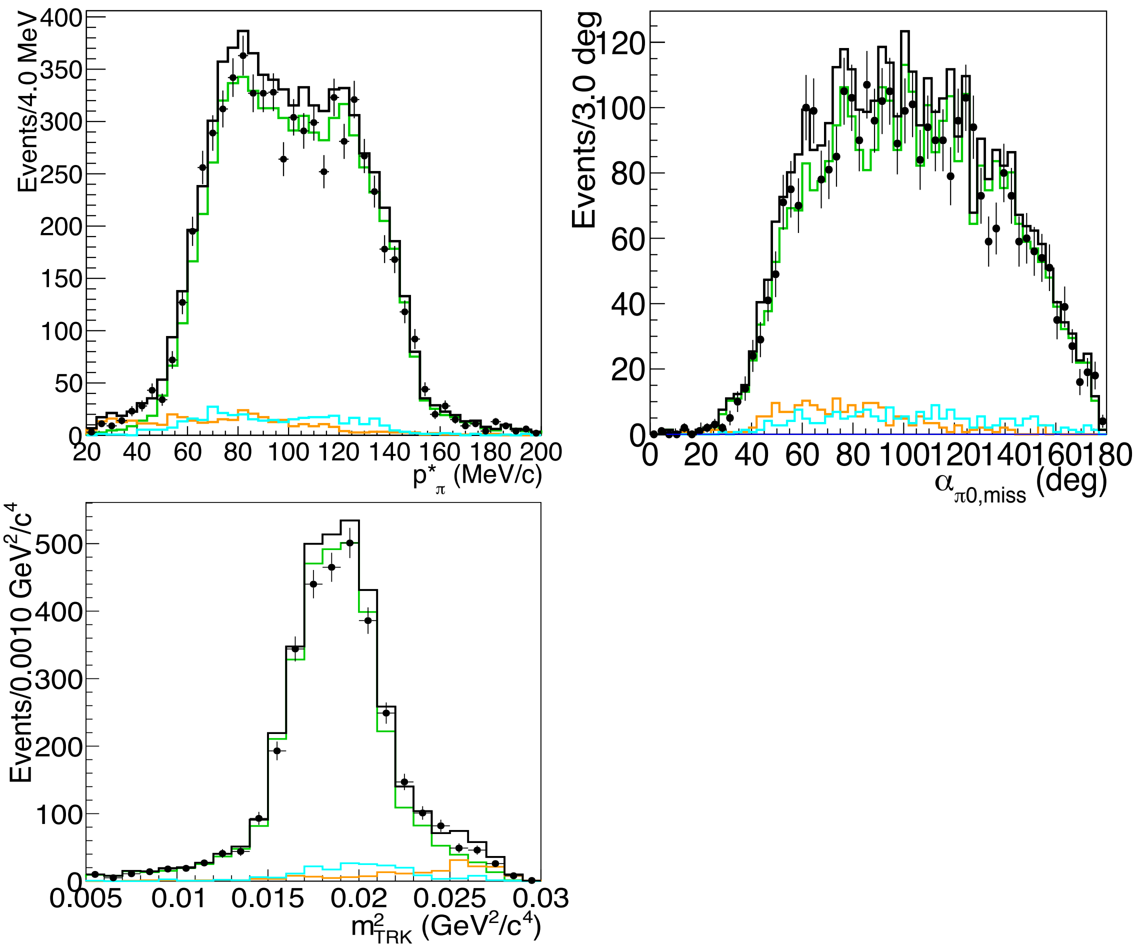

Figure 4.6: Distributions of p^*_π (top left), $\alpha_{\pi^0,\,\mathrm{miss}}$ (top right) and m^2_{TRK} (bottom left) in the CRKK region for data and predicted backgrounds after corrections. The different colored histograms represent the background categories: $\phi \to K^+K^-$ (green), $K_{\mathrm{S}} \to \pi^+\pi^-(\gamma)$ (red), $K_{\mathrm{S}} \to \pi^0\pi^0$ (orange), $\phi \to \pi^+\pi^0\pi^-$ (magenta), *Other* (cyan).

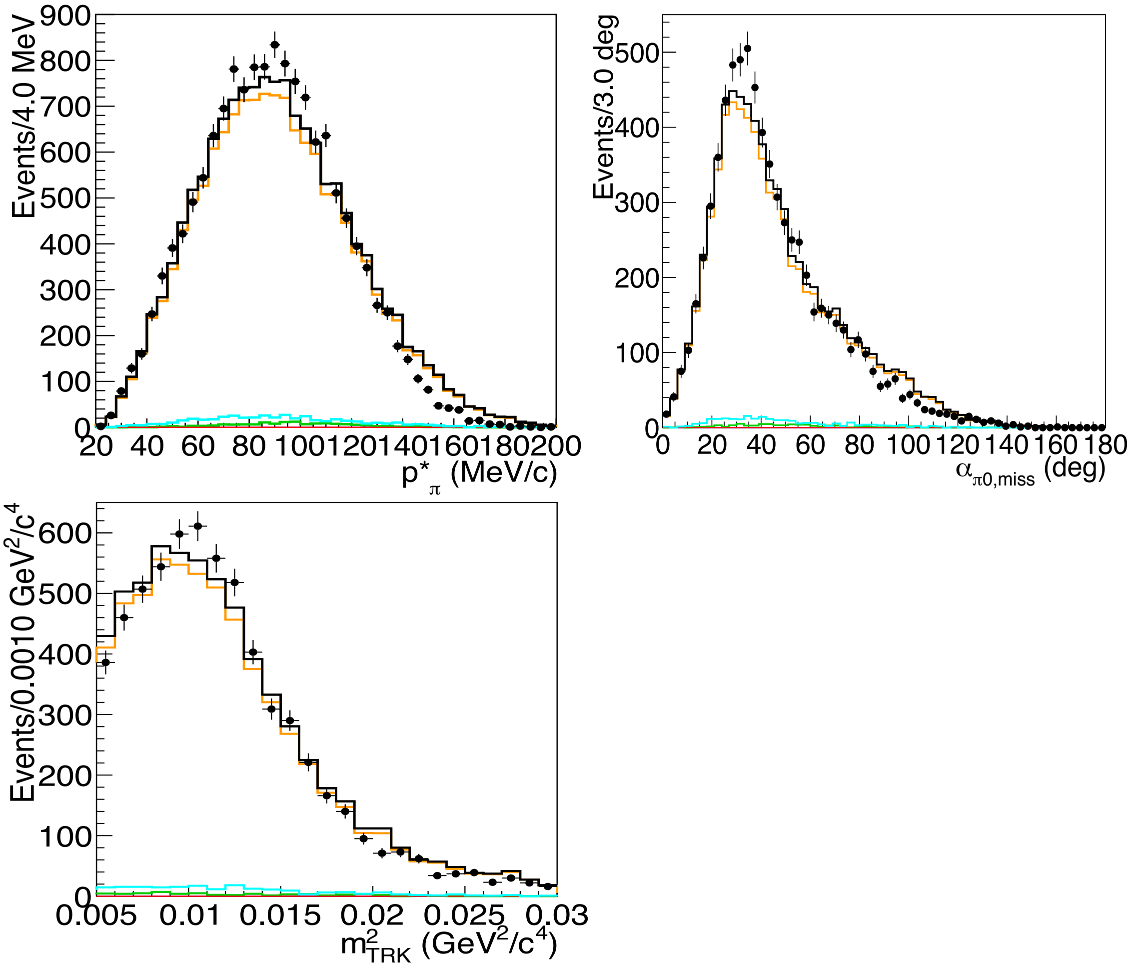

Figure 4.7: Distributions of p^*_π (top left), $\alpha_{\pi^0,\,\mathrm{miss}}$ (top right) and m^2_{TRK} (bottom left) in the CR2PI0 region for data and predicted backgrounds after corrections. The different colored histograms represent the background categories: $\phi \to K^+K^-$ (green), $K_\mathrm{S} \to \pi^+\pi^-(\gamma)$ (red), $K_\mathrm{S} \to \pi^0\pi^0$ (orange), $\phi \to \pi^+\pi^0\pi^-$ (magenta), *Other* (cyan).

Chapter 5

Determination of the branching ratio

The determination of the $K_S \to \pi^+\pi^0\pi^-$ branching ratio is described in this chapter. The fit procedure to the data distribution exploited to evaluate the normalization of signal and backgrounds events by using their MC shapes is also outlined. The signal counts are then evaluated once measured the signal distribution normalization. A discussion on systematic error sources is reported as well, together with some considerations on the possible strategy that could be adopted to minimize them, in view of a first direct and competitive measurement of the rare decay $K_S \to \pi^+\pi^0\pi^-$. We will first summarize the data analysis steps to have a complete overview of the whole analysis chain.

5.1 Data analysis summary

In order to select a pure K_S meson sample from ϕ-meson decays we have exploited the K_L-crash tag, described in sec. 3. This tagging algorithm has been used and extensively studied in previous KLOE analyses [45, 44, 46, 47, 48, 33]. In a sample of $N_{KS}^{TAG} = 5.26 \times 10^8$ tagged K_S mesons, the number of signal events predicted by the MC simulation is 5141. The following selections have been used to improve the signal to background ratio:

1. pre-selections, described in sec. 3.4: we have selected events with only 2 prompt clusters and only 2 tracks connected to a vertex reconstructed in a volume close

the the interaction region;

2. $0.205 < \beta^* < 0.225$, described in sec. 4.1.2;

3. $480 < M_{3\pi} < 520$, described in sec. 4.1.3.

Then, the signal box (SBOX) has been defined by exploiting the correlation $(\alpha_{\mathrm{LS}}, \alpha^*_{\pi\pi})$ (see sec. 4.2). The number of data, MC background and expected signal events is listed in Table 5.1 at each selection stage. The corresponding signal efficiencies from MC simulations are reported in Table 5.2. The total analysis efficiency is also listed in the last raw of this table.

Table 5.1: Number of events at each stage of selections, normalized to data integrated luminosity.

	Data	K^+K^-	$\pi^+\pi^-(\gamma)$	$\pi^0\pi^0$	$\phi \to \pi^+\pi^0\pi^-$	*Other*	Signal
Pre-sel	3483015	1519997	1238388	182766	360126	182101	45
β^* cut	658281	260187	132416	139466	63230	52461	35
$M_{3\pi}$ cut	20346	9035	24	14989	13	1038	33
SBOX	1003	565	4	381	1	45	30

Table 5.2: Signal efficiencies for each selection from MC simulation.

	Signal efficiency
Pre-selections	0.2622 ± 0.0061
β^* cut	0.779 ± 0.011
$M_{3\pi}$ cut	0.9314 ± 0.0078
SBOX definition	0.9151 ± 0.0089
Total	0.1741 ± 0.0053

5.2 Estimate of signal yield in the signal region

To evaluate the number of signal events in SBOX a simultaneous fit of the p^*_π, $\alpha_{\pi^0,\mathrm{miss}}$ and m^2_{TRK} distributions is performed, following the procedure described in ref. [49], an approach which takes into account the finite size of both data and MC samples. The meaning of the mentioned quantities has been described in sec. 4.2. The spectra of these variables are shown in fig. 5.1 for data, MC backgrounds and expected signal ($\times 10$). Since the most abundant background sources surviving the analysis are K^+K^- and $\pi^0\pi^0$, three MC background templates have been used to fit data:

- $\phi \to K^+K^-$;
- $K_S \to \pi^0\pi^0$;
- the sum of $\phi \to \pi^+\pi^0\pi^-$, $K_S \to \pi^+\pi^-(\gamma)$ and *Other* categories, called *residual* background hereafter.

The fitting procedure, using the three above mentioned MC background templates and signal spectra to fit data, allows to extract the fraction of data events, $f_j = n_j/N_D$, of the j-th category with the constraint $\sum_j f_j = 1$. The fractions of events returned by this simultaneous fit, performed in the range:

$$0^\circ < \alpha_{\pi^0,\mathrm{miss}} < 80^\circ \ \vee\ 30 < p^*_\pi < 160\,\mathrm{MeV}/c \ \vee\ 0.012 < p^*_\pi < 0.026\,\mathrm{GeV}^2/c^4\,,$$

are listed in Table 5.3. The number of signal events in data returned by the fit is $N_{\pi^+\pi^0\pi^-} = 39 \pm 15$. In fig.5.2 the fit result is shown for data, background and signal weighted by their fractions, f_j. Colored histograms represent background and signal contributions, which sum up to the total MC prediction represented by the black shaded histogram; black points are data.

Table 5.3: Fit results: fraction of events in data for each background category and for signal. The reduced χ^2 of the fit and the χ^2 probability are also reported.

f_{signal}	0.039 ± 0.015
$f_{K^+K^-}$	0.472 ± 0.067
$f_{\pi^0\pi^0}$	0.246 ± 0.071
f_{resid}	0.242 ± 0.052
χ^2/n_{dof}	1.022
$P(\chi^2)$	0.397

In order to cross-check the fit normalization of the background sources, we have listed in Table 5.4, first raw, the number of background events in SBOX corrected

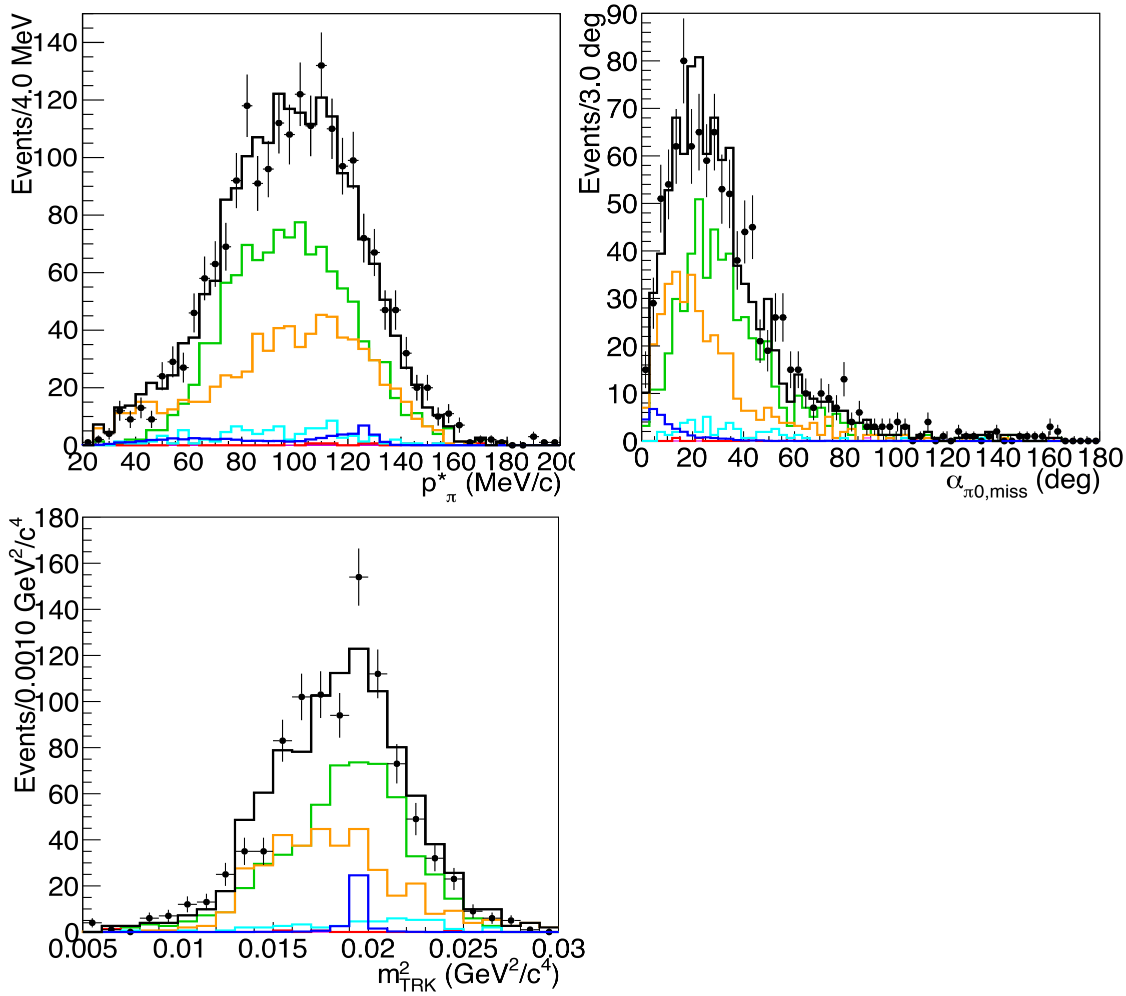

Figure 5.1: Distributions of p^*_π (top left), $\alpha_{\pi^0,\mathrm{miss}}$ (top right) and m^2_{TRK} (bottom left) in SBOX for data (black points), backgrounds and predicted signal (blue, $\times 10$). The different colored histograms represent the background-category templates used as input to the fit: $\phi \to K^+K^-$ (green), $K_S \to \pi^0\pi^0$ (orange), residual background (cyan). The black histogram is the sum of signal and backgrounds.

by the scaling factors derived in the two control regions CRKK and CR2PI0 (see sec. 4.2) and, in the second raw, the number of background events returned by the fit. For the residual background it has not been possible to define a control region as for the other two components, since this kind of events overlap with K^+K^- and $\pi^0\pi^0$ in the $(\alpha_{\mathrm{LS}}, \alpha^*_{\pi\pi})$ correlation plot. Therefore, in order to evaluate the expected normalization of this background, we proceeded by subtracting K^+K^- and $\pi^0\pi^0$ events from data events. As it is evident from Table 5.4, there is a nice agreement

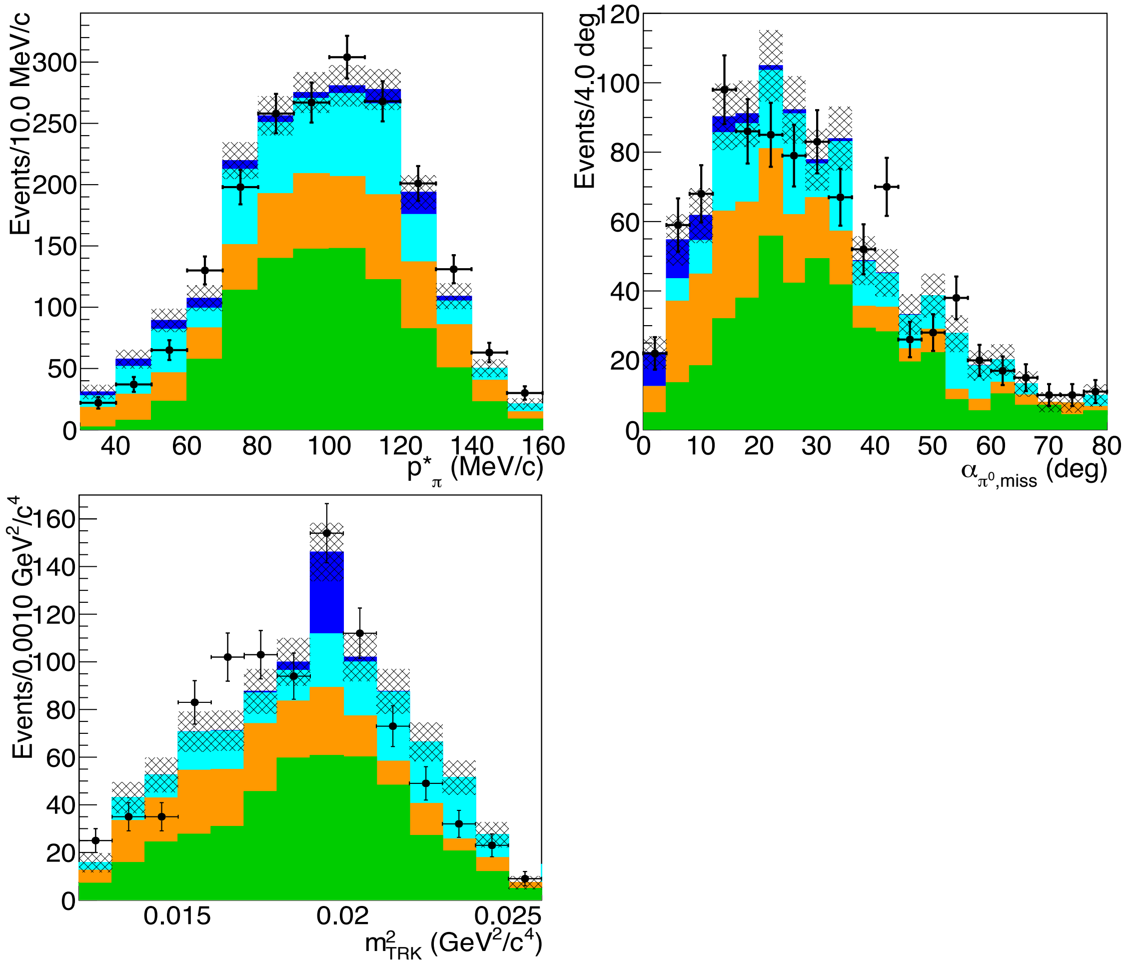

Figure 5.2: Distributions of p^*_π (top left), $\alpha_{\pi^0,\,\mathrm{miss}}$ (top right) and m^2_{TRK} (bottom left) after fit. Data are represented by black points, MC backgrounds and signal are represented by colored histograms: $\phi \to K^+K^-$ is green, $K_S \to \pi^0\pi^0$ is orange, residual background is cyan and signal is blue. The black shaded histogram is the sum of all MC background and signal contributions. Each source of background and the signal are normalized to the corresponding fractions given by the fit.

between the number of K^+K^- events expected by extrapolation and the fit output. The agreement is not preserved at the same level of accuracy for the $\pi^0\pi^0$ and residual backgrounds. This small discrepancy, which was expected by looking at the scaling factor $R^{\mathrm{CR}}_{\pi^0\pi^0}$ evaluated in the CR2PI0 region, also reflects in the difference between the number of expected and observed events for the residual background. Since the knowledge of the background is crucial when measuring a rare process, a deeper investigation will be done for a refined analysis.

Table 5.4: Comparison between the background events normalized as derived in the control regions (first raw) and as returned by the fit (second raw).

	K^+K^-	$\pi^0\pi^0$	Residual
CR's	496 ± 71	155 ± 45	369 ± 90
Fit	473 ± 67	247 ± 71	243 ± 52

5.3 Background-hypothesis fit in the signal region

A simultaneous fit of p^*_π, $\alpha_{\pi^0,\mathrm{miss}}$ and m^2_{TRK} distributions has been performed in the signal region, SBOX, in the background hypothesis. This allows us to check whether data are better fit considering both signal and backgrounds. The same procedure described in the previous section has been exploited: the input templates used to fit data in the background hypothesis are K^+K^-, $\pi^0\pi^0$ and residual background sources. Signal is not included among the input templates this time. Data have been fit using the same range as for the fit in the signal hypothesis described in previous section. The fit output is reported in Table 5.5. The residual background has been evaluated to be negligible compared to accuracy reported in the table and it is compatible with zero.

Table 5.5: Outcome of the background-hypothesis fit. The reduced χ^2 of the fit and the χ^2 probability are also reported.

$f_{K^+K^-}$	0.632 ± 0.046
$f_{\pi^0\pi^0}$	0.368 ± 0.045
f_{resid}	0.000 ± 0.021
χ^2/n_{dof}	1.110
$P(\chi^2)$	0.125

The fit in the background hypothesis points out that data are better fit if signal is included in the fit, as can be seen by comparing the reduced χ^2 and the χ^2 probability values of the fit reported in Tables 5.3 and 5.5. It is worth to notice that the number of residual background events is zero as given by the fit in the background hypothesis, being $f_{\mathrm{resid}} = 0.000 \pm 0.021$ as reported in Table 5.5. This is different from the expectation by analyzing the control regions CRKK and

CR2PI0, where the predicted number of residual background events turns out to be 369 ± 90, as reported in Table 5.4. This observed disagreement is due to the less consistent background hypothesis, which prevents the fit to correctly evaluate fractions of background events is data.

5.4 Branching ratio estimate

Given the number of tagged K_S mesons, $N_\mathrm{KS}^\mathrm{TAG}$, the branching ratio of the decay $K_\mathrm{S} \to \pi^+\pi^0\pi^-$ is obtained with the formula:

$$\mathscr{B}(K_\mathrm{S} \to \pi^+\pi^0\pi^-) = \frac{N_{\pi^+\pi^0\pi^-}}{N_\mathrm{KS}^\mathrm{TAG}\varepsilon_\mathrm{tot}},$$

where ε_tot is the total signal efficiency of the analysis, reported in Table 5.2. The branching ratio statistical uncertainty is computed as fractional error considering all terms in the above expression:

$$\left(\frac{\Delta\mathscr{B}}{\mathscr{B}}\right)^2 = \left(\frac{\Delta N_{\pi^+\pi^0\pi^-}}{N_{\pi^+\pi^0\pi^-}}\right)^2 + \left(\frac{\Delta N_\mathrm{KS}^\mathrm{TAG}}{N_\mathrm{KS}^\mathrm{TAG}}\right)^2 + \left(\frac{\Delta\varepsilon_\mathrm{tot}}{\varepsilon_\mathrm{tot}}\right)^2.$$

The branching ratio result is:

$$\mathscr{B}(K_\mathrm{S} \to \pi^+\pi^0\pi^-) = (4.3 \pm 1.6) \times 10^{-7},$$

where the statistical uncertainty is totally dominated by the error on the signal yield estimate.

5.5 Discussion on systematic uncertainties

The result on $\mathscr{B}(K_\mathrm{S} \to \pi^+\pi^0\pi^-)$ represents an absolute measurement, as we normalized the signal counts to the number of tagged K_S. Nevertheless, to get a more refined result we are going to use for the final measurement the ratio between $\mathscr{B}(K_\mathrm{S} \to \pi^+\pi^0\pi^-)$ and $\mathscr{B}(K_\mathrm{S} \to \pi^0\pi^0)$, the latter being known at percent level. This would allow a large cancellation of possible systematic uncertainties coming from K_L-crash tag requests and from the cut on β^*, never been used in previous KLOE analyses. We selected β^* in a window ranging from 0.205 to 0.225, to largely suppress background, while in all KLOE analyses it has been done in a wider range, $0.17 < \beta^* < 0.28$. This wide range has not been used. As already discussed in chapter 4, the MC simulation shows that the $\pi^+\pi^0\pi^-$ signal is peaked around the $\pi^0\pi^0$ signal rather than the $\pi^+\pi^-$, because the trigger is given by the fastest particles. The peak is well reproduced by the MC since the trigger is synchronized to the beam-beam crossing time, but the tails of the distribution may differ between $\pi^+\pi^0\pi^-$ and $\pi^0\pi^0$. To investigate this effect, the analysis should be done varying the β^* cut, by selecting larger portions of the tails.

The systematic contribution coming from the usage of MC shapes for both signal and background contributions has to be estimated. This has been done by changing both the signal box selection and the control regions definition.

Using MC to evaluate the tracking and vertexing efficiencies, as well as the photon detection efficiency, may also introduce systematic errors in the analysis. These sources of systematics have been studied in many KLOE analyses and we can directly compare to them. Control samples will be used to measure these efficiencies directly on data, e.g. $\phi \to \eta\gamma$, $\eta \to \pi^+\pi^0\pi^-$, in order to estimate the corresponding systeamtics.

Other sources of systematic uncertainties are trigger, FILFO and cosmic veto efficiencies. These have been exhaustively studied in all KLOE analyses and, thus, we have a direct comparison to them. They will be anyway measured for a refined measurement.

In order to evaluate the systematic uncertainty coming from the analysis cuts (i.e. the SBOX definition, the $m_{3\pi}$ cut and the β^* cut) we have performed a stability study of the measured branching ratio by varying one cut a time, keeping all the others fixed. For each selection configuration we have repeated the whole analysis and extracted a value of the branching ratio.

SBOX definition variation The boundaries of the signal box:

$$80^\circ < \alpha^*_{\pi\pi} < 180^\circ \quad \vee \quad 150^\circ < \alpha_{LS} < 180^\circ\,,$$

have been changed in order to allow for the MC shapes to change and test the fit response stability while changing the amount of background entering the signal region. Both the boundaries of the signal box have been changed at each step of this stability study. The total amount of background entering the

SBOX has been changed up to 60% in absolute value, corresponding to a cut variation of about ± 2 standard deviations in both α_{LS} and $\alpha^*_{\pi\pi}$. The resulting systematics has been evaluated as the RMS of the obtained result (fig. 5.3, left): $\delta_{\mathrm{SBOX}} = 0.7 \times 10^{-7}$.

$\mathbf{m_{3\pi}}$ cut variation The cut on the three-pion mass has been vaired to change by $\pm 50\%$ the amount of background entering the signal box, corresponding to a cut variation of about 2 standard deviations in $m_{3\pi}$. The resulting systematics has been evaluated as the RMS of the obtained result (fig. 5.3, center): $\delta_{m_{3\pi}} = 0.7 \times 10^{-7}$.

$\boldsymbol{\beta^*}$ cut variation The β^* cut interval has been varied in a such a way that large portions of the MC signal distribution tails were included in the selection of the events. As a consequence, larger amounts of background, especially $\pi^+\pi^-(\gamma)$ and K^+K^-, have entered the signal box. The total background variation, in absolute value, is 60% for this stability study. The resulting systematics has been evaluated as the RMS of the obtained result (fig. 5.3, right): $\delta_{\beta^*} = 0.7 \times 10^{-7}$.

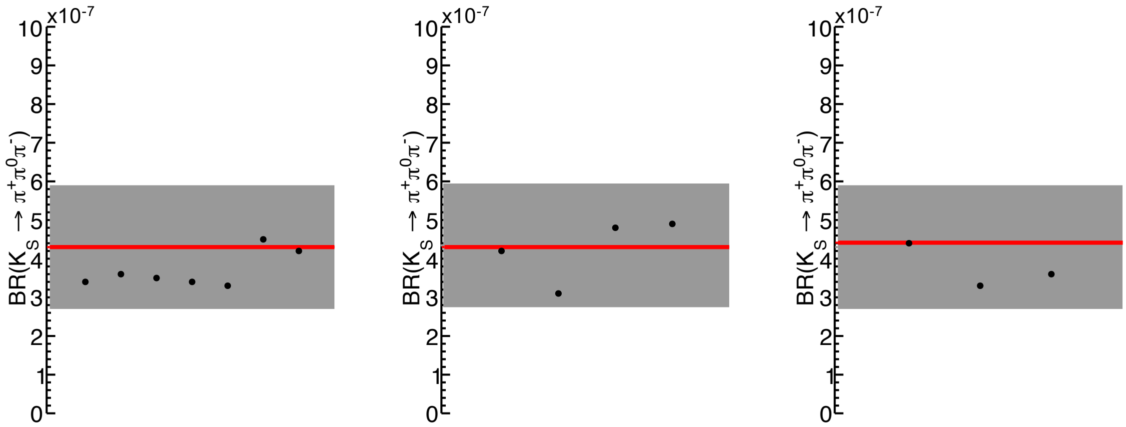

Figure 5.3: Variation of the measured branching ratio as a function of the SBOX definition variation (left), of the $m_{3\pi}$ cut variation (center), of the β^* cut variation (right). Red lines represent the branching ratio value measured with the standard analysis cuts. Grey bands represent the statistical uncertainty.

The total systematic uncertainty due to the variation of the analysis cuts has been evaluated as the sum in quadrature of each contribution reported above: $\delta_{syst} = 1.2 \times 10^{-7}$.

The branching ratio measurement is:

$$\mathscr{B}(K_S \to \pi^+\pi^0\pi^-) = (4.3 \pm 1.6_{\text{stat}} \pm 1.2_{\text{syst}}) \times 10^{-7} .$$

Table 5.6 lists the branching ratio values measured by E621 [9], NA48 [11] and CPLEAR [10] experiments compared to our result, that is the first direct measurement of the rare decay $K_S \to \pi^+\pi^0\pi^-$.

Table 5.6: KLOE preliminary measurement is compared to existing ones by E621, NA48 and CPLEAR experiments.

	BR $\times 10^{-7}$	Stat. Uncertainty	Syst. Uncertainty
KLOE preliminary	4.3	± 1.6	± 1.2
E621	4.8	${}^{+2.2}_{-1.6}$	± 1.1
NA48	2.5	${}^{+1.3}_{-1.0}$	${}^{+0.5}_{-0.6}$
CPLEAR	4.7	${}^{+2.2}_{-1.7}$	${}^{+1.7}_{-1.5}$

Conclusions

The first absolute measurement of the branching ratio of the rare decay $K_\mathrm{S} \to \pi^+\pi^0\pi^-$ has been presented in this thesis. We have exploited the tagging technique, a unique feature of a ϕ-factory, which allows to select a pure K_S beams by identifying the K_L interaction in the calorimeter. Within a sample of 5.26×10^8 tagged K_S mesons, we extracted the signal yield by fitting the data with the MC spectra of signal and background contributions entering the signal region, improving the initial background-to-signal ratio from about 8×10^4 to 33 with the selections described in chapters 3 and 4. We obtained a branching ratio value of $(4.3 \pm 1.6_\mathrm{stat} \pm 1.2_\mathrm{syst}) \times 10^{-7}$, with a 37% statistical accuracy on the measurement. It represents the first direct measurement of this branching ratio and the achieved accuracy is competitive compared to the precision of the few, all indirect, available measurements.

Systematic uncertainties from signal selection cuts have been evaluated by changing the analysis cuts. The present accuracy on the measurement due to systematics is 28%. Based on previous KLOE analysis, using a similar approach to evaluate systematics originating from other sources, we do not expect significant changes in the total systematic uncertainty which is going to be evaluated for a refined measurement.

A roadmap to obtain a more sophisticated measurement of the branching ratio of the $K_\mathrm{S} \to \pi^+\pi^0\pi^-$ rare decay, based on the normalization to the number of $K_\mathrm{S} \to \pi^0\pi^0$ events in the same K_S-tagged sample, has been also presented, together with some indications on the possible strategy to refine the analysis.

What next: KLOE-2

This chapter is focused on a different topic with respect to the rest of the thesis. The KLOE upgrade is central in the following paragraphs, whose main subject is the Inner Tracker cylindrical-GEM detector of the KLOE-2 experiment.

Overview

KLOE-2 is the main experiment of the INFN Frascati National Laboratories (LNF) and represents the continuation of the KLOE experiment, upgraded with state-of-the-art technology to improve its discovery potential. The new data taking campaign will allow to perform discrete symmetry and quantum coherence tests using neutral kaons with an unprecedented accuracy, high precision studies of $\gamma\gamma$-physics processes, such as $e^+e^- \to e^+e^-\pi^0$ ($\gamma\gamma \to \pi^0$), and to search for new exotic particles that could constitute the dark matter [23]. To this extent, the previous experimental apparatus described in chapter 2, consisting of a large Drift Chamber (DC) and an Electromagnetic Calorimeter (EMC), both immersed in a 0.52 T axial magnetic field, undergone several upgrades including a novel cylindrical-GEM detector, the Inner Tracker, to improve track and vertex reconstruction capabilities near the interaction region.

KLOE-2 is the first high-energy experiment using the GEM technology with a fully-cylindrical geometry, a novel idea that was developed at LNF exploiting the kapton properties to build a light and compact tracking system. State-of-the-art solutions have been expressly developed or tuned for this project: single-mask GEM etching, multi-layer readout circuit, PEEK spacer grid, GASTONE front-end chip and General Interface Board electronics. The Inner Tracker (IT) was mounted on DAΦNE beam pipe and inserted inside the KLOE apparatus in July 2013 with the commissioning phase starting late January 2014. Alignment and calibration of a cylindrical GEM detector was never done before and represents one of the challenging activities of the experiment.

KLOE-2 started its first data taking campaign in November 2014, acquired 2.4 fb^{-1} by December 2016 and is presently restarting data taking with the aim of collecting more than 5 fb^{-1} in the next 1-2 years. Record performance in terms of 2×10^{32} $\text{cm}^{-2}\text{s}^{-1}$ peak luminosity and 13 pb^{-1} maximum daily integrated luminosity were achieved with the innovative *crab-waist* beam collision scheme, developed in Frascati, which will be employed in the upgrade of the B-factory currently under construction at the KEK Laboratory in Japan and is considered a valid option in several future projects.

Inner Tracker detector description

To improve the resolution on decay vertices close to the interaction point (IP), reconstructed from low-momentum charged secondaries, the IT has been inserted in the free space between the beam pipe and the inner wall of KLOE DC. This new ultra-light detector, with its total material budget below 2% of the radiation length X_0, allows to minimize dead spaces and to limit the multiple scattering of low-momentum tracks and the probability of photon conversions at KLOE-2. The resolution on vertices close to the IP is expected to improve of about a factor 2-3 [50].

The IT is composed by four concentric cylindrical GEM (CGEM) detector layers, at radii from 13 cm, to preserve the K_L-$K_\text{S}$quantum interference region, to 20.5 cm due to the constraints from DC inner wall. The total active length for all layers is 70 cm. Fig. 4 left shows the four layers before assembling the Inner Tracker. Each CGEM [51] is a triple-GEM detector made of five concentric cylindrical electrodes (fig. 4, right): the cathode, to set the drift field, 3 GEM foils for the electron multiplication and the anode, acting also as readout circuit.

The R&D phase included the tuning and development of a new manufacturing procedure of GEM foils of unprecedented size (up to 50×100 cm^2) with a single-mask electro-chemical etching of the micro-holes, produced with the TE-MPE-EM CERN group. This activity has been followed and supported within the RD51 Collaboration [52].

The anode readout is patterned with longitudinal X strips with 650μm pitch, interleaved, on the same substrate and at the same level, with pads connected through

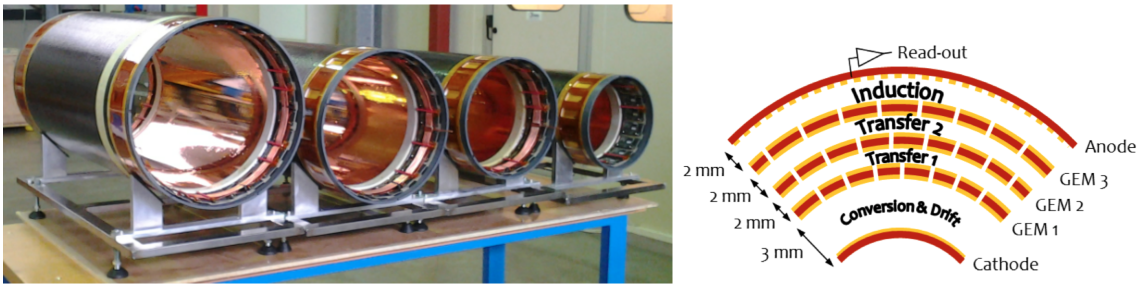

Figure 4: *Left:* the four layers of the Inner Traker. *Right*: cross-section of a triple-GEM IT layer.

internal vias to form V strips at an angle within 25°÷27° and with 600 μm pitch, for a total of about 30,000 FEE channels. Space coordinates are reconstructed using this dedicated XV strips patterned readout coupled to the GASTONE front-end, the 64-channel ASIC with digital output developed for the KLOE-2 experiment [53]. Data collection is then performed with a General Interface Board (GIB) with a configurable FPGA architecture, Gigabit Ethernet and the readout driver (ROD), also developed for KLOE-2 [54].

An Ar/iC_4H_{10} 90:10 gas mixture was chosen among other mixtures to account for relevant operating parameters such as discharge probability measured with α-particles

In the following we use a coordinate system with the z-axis defined as the bisector of the e^+e^- beams, the y-axis vertical and the x-axis toward the center of the collider rings. The IT axis is along the z-axis and therefore the X-view strips are parallel to this axis.

Detector operation

After three years of R&D [55, 56, 57], which demonstrated the feasibility of a cylindrical triple-GEM detector with an XV readout, the construction of the KLOE-2 Inner Tracker was completed in March 2013. In June 2013 the IT was integrated on DAΦNE beam pipe and equipped with two cooling systems: copper coils as water radiators on the front-end electronics and air blowing on the IT end-caps and between the beam-pipe and the IT innermost layer. The Inner Tracker was finally inserted inside the KLOE-2 apparatus in July 2013.

The optimization of the IT operational parameters with colliding beams started in late 2014 during the first KLOE-2 data taking campaign, as a function of the e^+e^- beam currents and machine background conditions.

In order to measure efficiency and resolutions, dedicated procedures were developed exploiting the Drift Chamber track reconstruction and using cosmic-ray muon data and Bhabha scattering events. The IT optimal working point was set with single-view and two-view efficiency up to 98% and 95% respectively.

Switching on the detector with e^+e^- collisions from DAΦNE, a clear correlation between beam injections and IT measured currents was observed. To this extent the machine background conditions have to be monitored and carefully kept under control. Dedicated online monitoring procedures were developed and are currently used to check IT temperature, currents and voltages, together with occupancy and clustering performance [58] with DAΦNE delivering collision data.

To safely operate all KLOE-2 sub-detectors and for e^+e^- injection optimization, the information from three indicators of the machine background level is sent online to DAΦNE operators: the current measured on the first IT layer, the total current measured in the DC and the background level measured in the calorimeter end-caps. This allowed machine background conditions to be kept at an acceptable level having at the same time good collider uptime and luminosity performance.

The detector status must be monitored in time and during data acquisition. Proper masking of noisy front-end electronic channels and the identification of dead strips is fundamental to correctly evaluate the detector efficiency and to monitor and account for detector condition on a run-by-run basis at the analysis stage. The definition of *noisy* and *dead* strips is related to the average occupancy for a single view and for each layer of the Inner Tracker as obtained with cosmic-ray muon data.

Dedicated runs are acquired every 2-3 days for detector calibration and status monitoring: these include cosmic-ray muon samples for all sub-detectors. An automated procedure evaluating noisy and dead strips in the IT has been developed and its output written into the database to be used at the reconstruction stage. From a reference cosmic-ray muon run we have few % of noisy strips and some % of dead strips, considering both views and all the four layers. Dead strips are mainly due to anomalous DAΦNE beam injections or unexpected beam losses. The source has been found in the HV sectorization which creates a distortion of the electric field resulting in higher effective gain at the edges of HV micro-sectors. A safer operation of the IT has been reached with:

- the optimization of beam injections by the DAΦNE team with KLOE-2 online feedback information, mainly DC and IT currents;
- a new HV distribution scheme with an individual floating channel system and single voltages adjustment, developed together with CAEN, which prevents propagation of possible discharge with anomalous injections.

Efficiency measurment

The Inner Tracker efficiency is evaluated with cosmic-ray muon tracks reconstructed in the DC: tracks are extrapolated to the Inner Tracker and all events in which they cross the IT layers at two points are selected as normalization sample for efficiency measurement.

High voltage scans have been performed setting different induction field values, namely 5 kV/cm and 6 kV/cm. A single-view efficiency up to 98% has been measured by setting the induction field to 6 kV/cm, as reported in Fig. 5 for Layer 1.

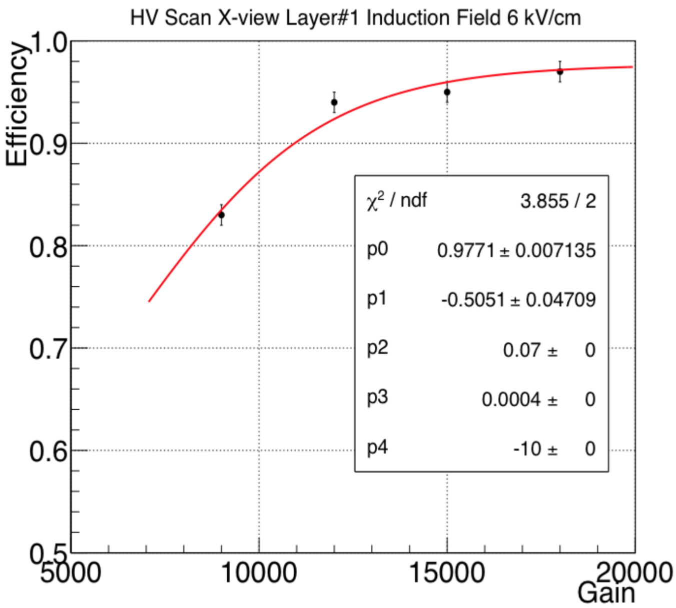

Figure 5: Layer 1 single-view efficiency as a function of the effective gain. Black points are experimental data, while the solid line is the Fermi-Dirac best fit curve.

A satisfactory 95% two-view efficiency has been measured. All layers provide similar results. Presently the IT is operated with a nominal gain of 1.2×10^4, with electric fields set at 1.5/3/3/6 kV/cm and GEM1/GEM2/GEM3 voltages set at 285/280/265 V. These values were chosen as a good compromise between detector efficiency and safe operation with collisions.

Alignment and Calibration

In order to properly perform track reconstruction using the IT information, alignment and calibration of this detector should be first performed.

Two effects with $\mathcal{O}(1-2\text{ mm})$ average corrections were observed and measured with planar XV prototypes at the test beams during the R&D phase of the project [50]. The first effect is related to non-radial tracks crossing the IT as shown in fig. 6. Due to the angle β between the electric field drift line direction and the

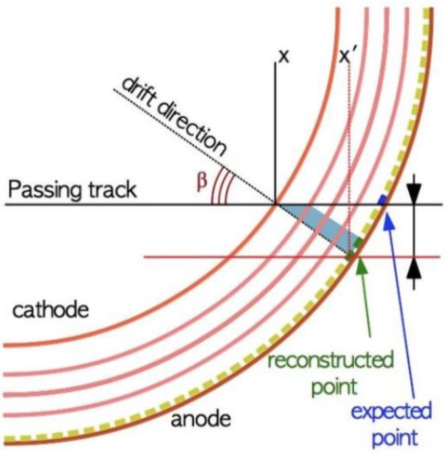

Figure 6: Non-radial tracks effect sketch.

incident track, the crossing point between the incident track and the anode plane, the *expected position*, will be shifted to the *reconstructed point* and the signal electron cloud will be spread. The second effect is due to the presence of the magnetic field. Also in this case there will be a shift and a spread of the signal electron cloud, experiencing the Lorentz force. T he combination of these two effects produces a focusing or defocusing of the electron cloud according to the impact parameter of the track on the cylindrical detectors. These effects must be studied and measured independently: cosmic-ray muon data have been used to evaluate the non-radial correction (without B-field) and the magnetic field influence (with B-field), and

Bhabha scattering events to check the effect of the two corrections.

The alignment and calibration of the IT is performed with respect to DC reconstructed tracks, providing the *expected position* on each IT layer. The figure of merit is given by the residual distribution defined as the difference between *expected position* and 3D IT cluster *reconstructed point*, along the three coordinates.

A first set of alignment and calibration parameters was obtained with cosmic-ray muons without B-field, selecting DC tracks with Point of Closest Approach (PCA) to the beam line with transverse radius $R_{PCA} < 5$ cm and $p_T > 500$ MeV, extrapolated to the IT with the straight-line approximation. As an example, the starting point for the residual widths and mean values of Layer 4 without any alignment or calibration were: Res(x)$\sim$ 1.5 mm, Res(y) $\sim$ 280 μm, Res(z) $\sim$ 3.6 mm and $\Delta x \sim 860$ μm, $\Delta y \sim$ -50 μm $\Delta z \sim 2$ mm. The results after the first alignment and calibration for all layers exhibit average residual widths along the x-axis Res(x) $\sim$ 400 μm for all layers but Layer 1 exhibiting 700 μm, along the z-axis Res(z) $\sim$ 1 mm and the all residual distributions centered around zero within 50 μm. The alignment and calibration includes shifts, rotations and corrections as a function of θ and ϕ angles of the DC track. The preliminary results of about 400 μm are within expectations for the Inner Tracker resolution.

Starting from the B-field Off sample parameters, a first set of calibration parameters for the cosmic-ray muon sample with B-field was obtained with average value Res(x) $\sim$ 550 μm for all layers but Layer 1 exhibiting Res(x) $\sim$740 μm. The calibration includes residual non-radial track effect correction as a function of the β angle and an average correction for the B-field effect.

Finally both corrections for non-radial track and B-field effect, obtained with cosmic-ray muon samples, have been cross-checked with Bhabha scattering events. The average residuals are Res(x) $\sim$ 400 μm for all layers but Layer 1 exhibiting Res(x) $\sim$500 μm.

Fig. 7 shows the path towards the first alignment and calibration results of the IT Layer 4: starting from the 1.5 mm residual width of the cosmic-ray muon B-field Off sample without alignment and calibration (top left) to the 440 μm of the same sample with the first alignment and calibration for B-field Off (top right), passing to 560 μm obtained with the first calibration of the cosmic-ray muon B-field On sample (bottom left) to arrive to the 400 μm obtained applying previous alignment and calibration parameters to Bhabha scattering events (bottom right). This validates our method and also suggests how to improve the alignment and calibration procedure in order to reach the best detector performance: we have to introduce the correction as a function of the β angle starting from the cosmic-ray muon sample without B-field.

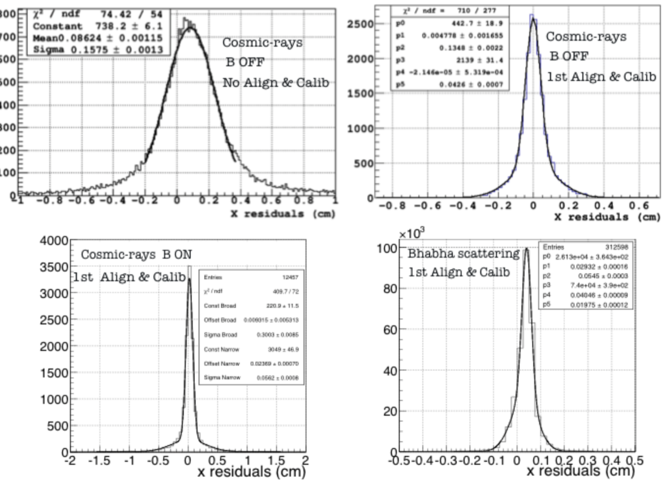

Figure 7: Non-radial tracks effect sketch.

Track reconstruction

Starting from DC hits and track reconstructed parameters, IT clusters are included by using the Kalman filter technique and then track parameters updated accounting for the additional IT information. Bhabha scattering events, selected as in the alignment and calibration procedure, are used as benchmark. First the alignment and calibration parameters obtained with the cosmic-ray muon sample with magnetic field On are inserted, accounting for both non-radial track and B-field effects. Then, for each DC track, the corrections parametrized as a function of ϕ and θ angles of the track (Non-radial track effect) and as a function of the β angle together with an average B-field correction (B-field effect) are applied. Therefore the calibrated IT clusters are used for IT+DC integrated tracking.

To validate the insertion of these corrections in the official reconstruction software, we evaluate the residual distribution with the same procedure used in the standalone code developed for alignment and calibration: the residual is defined as the difference between the DC extrapolated track and the closest IT cluster. After this validation, the calibrated clusters can be used in the IT+DC integrated track-

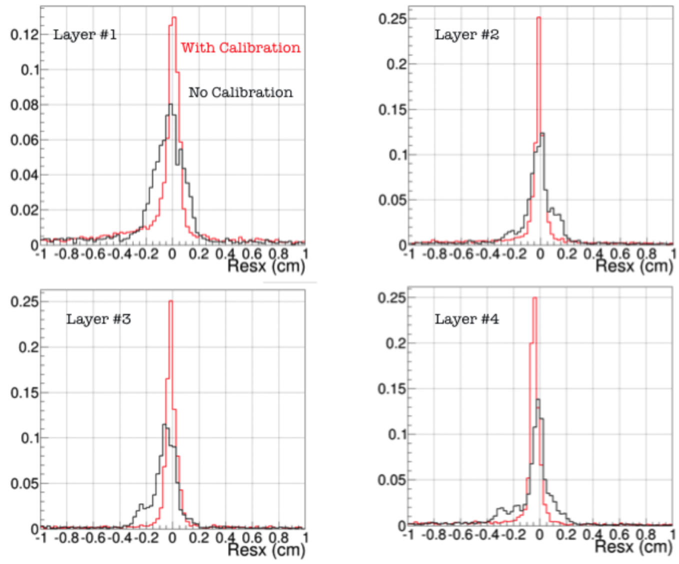

Figure 8: Residuals between IT clusters and expected position from Kalman with (red) and without (black) calibration.

ing. The residual distributions between the IT clusters and the expected position from the Kalman filter, with and without the calibration, have been evaluated for each layer. The improvement obtained with the calibration is shown in Fig. 8, where all IT clusters within 5 cm from the extrapolated track have been used.

With the first calibration, the IT cluster measurements can be fully exploited in the Kalman filter. First studies have been performed using Bhabha scattering events, selected using Level-3 pre-scaled events, and with a simple vertex finder based on minimum distance between extrapolated tracks, with DC only and using the integrated IT+DC tracking. This in not the official vertexing of the experiment. A very preliminary study demonstrated that, e.g., the average resolution on the x coordinate of the output of the simple vertex finder obtained using DC tracks only is about 2 cm, while using the very first version of the integrated tracking IT+DC adding IT preliminary calibrated clusters it is about 1.3 cm.

We are presently working on the refinement of the the calibration constants for all IT layers, as well as on the IT+DC integrating tracking, in order to exploit the great potential of this GEM detector in future KLOE-2 analyses. Enhanced reconstruction capabilities close to the interaction region will allow us to study all those decays occurring near the interaction point with higher accuracy then in the past. The measurement of the rare decay $K_S \to \pi^+\pi^0\pi^-$ will definitely profit of the presence of the Inner Tracker in the KLOE-2 apparatus.

Bibliography

[1] E. Noether, Nachrichten von der Gesellschaft der Wissenschaften zu Göttingen, Mathematisch-Physikalische Klasse pp. 37–44 (1918).

[2] C. S. Wu, E. Ambler, R. W. Hayward, D. D. Hoppes, and R. P. Hudson, Physical Review **105**, 1413 (1957).

[3] R. L. Garwin, L. M. Lederman, and M. Weinrich, Physical Review **105**, 1415 (1957).

[4] J. H. Christenson, J. W. Cronin, V. L. Fitch, and R. Turlay, Physical Review Letters **13**, 138 (1964).

[5] N. Cabibbo, Physical Review Letters **10**, 531 (1963).

[6] M. Kobayashi and T. Maskawa, Progress of Theoretical Physics **49**, 652 (1973).

[7] G. Anzivino et al., Journal of Physics: Conference Series **335**, 012015 (2011).

[8] A. Alavi-Harati et al., Physical Review D **67**, 012005 (2003).

[9] Y. Zou et al., Physics Letters B **369**, 362 (1996).

[10] R. Adler et al., Physics Letters B **407**, 193 (1997).

[11] J. R. Batley et al., Physics Letters B **630**, 31 (2005).

[12] G. D. Rochester and C. C. Butler, Nature **160**, 855 (1947).

[13] M. Gell-Mann, Physical Review **92**, 833 (1953).

[14] M. Gell-Mann and A. Pais, Physical Review **97**, 1387 (1955).

[15] B. Winstein and L. Wolfenstein, Reviews of Modern Physics **65**, 1113 (1993).

[16] T. D. Lee and C. N. Yang, Physical Review **104**, 254 (1956).

[17] T. D. Lee, R. Oehme, and C. N. Yang, Physical Review **106**, 340 (1957).

[18] C. S. Wu, E. Ambler, R. W. Hayward, D. D. Hoppes, and R. P. Hudson, Physical Review **105**, 1413 (1957).

[19] L. Landau, Nuclear Physics **3**, 127 (1957).

[20] K. A. Olive et al. (Particle Data Group), Chin. Phys. **C38**, 090001 (2014).

[21] L. Maiani et al., *The Second DAΦNE Physics Handbook* (SIS - Pubblicazioni dei Laboratori Nazioni di Frascati, 1995).

[22] E. Aslanides, Proceedings of XIV International Conference of Physics in Collisions **365** (1995).

[23] G. Amelino-Camelia et al., The European Physical Journal C **68**, 619 (2010).

[24] J. Bernabéu, N. Mavromatos, and J. Papavassiliou, Physical Review Letters **92**, 131601 (2004).

[25] J. Bernabéu, N. E. Mavromatos, and S. Sarkar, Physical Review D **74**, 045014 (2006).

[26] G. B. Thomson and Y. Zou, Physical Review **51**, 1412 (1995).

[27] E. Abouzaid et al., Physical Review D - Particles, Fields, Gravitation and Cosmology **83**, 1 (2011).

[28] D. Babusci et al., Physics Letters B **730**, 89 (2014).

[29] D. H. Perkins, *Introduction to High Energy Physics* (Addison-Wesley Publishing Company, Inc., 1972).

[30] S. Fajfer and J. M. Gerard, Zeitschrift fur Physik C Particles and Fields **42**, 425 (1989).

[31] H.-Y. Cheng, Physics Letters B **238**, 399 (1990).

[32] J. Kambor, J. Missimer, and D. Wyler, Physics Letters B **261**, 496 (1991).

[33] D. Babusci et al., Physics Letters B **723**, 54 (2013).

[34] L. Lavoura, Modern Physics Letters A **7**, 1367 (1992).

[35] F. Bossi, E. De Lucia, J. Lee-Franzini, S. Miscetti, M. Palutan, and KLOE Collaboration, Rivista del Nuovo Cimento **31**, 531 (2008).

[36] M. Adinolfi et al., Nuclear Instruments and Methods in Physics Research A **488**, 51 (2002).

[37] M. Adinolfi et al., Nuclear Instruments and Methods in Physics Research A **494**, 326 (2002).

[38] M. Adinolfi et al., Nuclear Instruments and Methods in Physics Research A **492**, 134 (2002).

[39] F. Ambrosino et al., Nuclear Instruments and Methods in Physics Research A **534**, 403 (2004).

[40] M. L. Ferrer and KLOE Collaboration, Proceedings of Int. Conf. on Advances in Infrastructure for Electronics, Business, Science and Education on the Internet, L'Aquila, Italy (2002).

[41] F. Ambrosino et al., KLOE Memo **255** (2000).

[42] F. Ambrosino et al., European Physical Journal C **47**, 589 (2006).

[43] S. Sinibaldi and T. Spadaro, KLOE Memo **146** (2004).

[44] F. Ambrosino et al., European Physical Journal C **48**, 767 (2006).

[45] F. Ambrosino et al., Physics Letters B: Nuclear, Elementary Particle and High-Energy Physics **619**, 61 (2005).

[46] F. Ambrosino et al., Physics Letters B: Nuclear, Elementary Particle and High-Energy Physics **636**, 173 (2006).

[47] F. Ambrosino et al., Journal of High Energy Physics **05**, 51 (2008).

[48] F. Ambrosino et al., Physics Letters B **672**, 203 (2009).

[49] R. Barlow and C. Beeston, Computer Physics Communications **77**, 219 (1993).

[50] F. Archilli et al., arXiv:1002.2572v1 and LNF-10/3(P) INFN-LNF, Frascati (2010).

[51] G. Bencivenni and D. Domenici, Nuclear Instruments and Methods in Physics Research A **581**, 221 (2007).

[52] M. Alfonsi et al., Nuclear Instruments and Methods in Physics Research A **617**, 151 (2010).

[53] F. Loddo et al., Nuclear Instruments and Methods in Physics Research A **721** (2013).

[54] P. Branchini et al., Journal of Instrumentation **8**, T04004 (2013).

[55] G. Bencivenni et al., Nuclear Instruments and Methods in Physics Research A **698**, 185 (2013).

[56] A. Balla et al., Journal of Instrumentation **9**, C01014 (2014).

[57] A. Balla et al., Nuclear Instruments and Methods in Physics Research A **628**, 194 (2011).

[58] A. Di Cicco and G. Morello, Acta Physica Polonica B **46** (2015).